Improvement of Airborne Retrievals of Cloud Droplet Number Concentration of Trade Wind Cumulus Using a Synergetic Approach

Kevin Wolf[1], André Ehrlich[1], Marek Jacob[2], Susanne Crewell[2], Martin Wirth[3], and Manfred Wendisch[1]

[1]Leipzig Institute for Meteorology, University of Leipzig, Leipzig, Germany

[2]Institute for Geophysics and Meteorology, University of Cologne, Cologne, Germany

[3]Institute of Atmospheric Physics, German Aerospace Center, Oberpfaffenhofen, Germany

Correspondence to: K. Wolf (kevin.wolf@uni-leipzig.de)

Abstract. In-situ measurements of cloud droplet number concentration N are limited by the sampled cloud volume. Satellite retrievals of N suffer from inherent uncertainties, spatial averaging, and retrieval problems arising from the commonly assumed strictly assume adiabatic vertical profiles of cloud properties. To improve retrievals of N it is suggested in this paper to use a synergetic combination of passive and active airborne remote sensing measurement, to reduce the uncertainty of N retrievals and to bridge the gap between in-situ cloud sampling and global averaging. For this purpose, spectral solar radiation measurements above shallow trade wind cumulus were combined with passive microwave and active radar and lidar observations carried out during the second Next Generation Remote Sensing for Validation Studies (NARVAL-II) campaign with the High Altitude and Long Range Research Aircraft (HALO) in August 2016. The common technique to retrieve N is refined by including combined measurements and retrievals of cloud optical thickness τ, liquid water path LWP, cloud droplet effective radius r_{eff}, as well as cloud base and top altitude. Three approaches are tested and applied to synthetic measurements and two cloud scenarios observed during NARVAL-II. Using the new combined retrieval technique, errors in N due to the adiabatic assumption have been reduced significantly.

1 Introduction

Clouds influence the Earth's radiative energy budget by reflecting, absorbing, and emitting solar and terrestrial radiation. These effects are typically quantified by the cloud radiative forcing (CRF), which is defined by the difference between the net radiation (downward minus upward irradiance) in cloudy and cloud-free conditions. Depending on the cloud type, the cloud optical and microphysical properties, as well as their spatial and temporal occurrence, the CRF can vary significantly (Rosenfeld, 2006). In the tropics, clouds can either cool or warm the atmosphere / surface below the cloud. While for cirrus a warming effect dominates (Wendisch et al., 2007), boundary layer trade wind cumuli typically cool the subjacent atmosphere / surface by efficiently reflecting solar radiation (Warren et al., 1988). Therefore, a realistic representation of clouds in numerical weather prediction (NWP) and global climate models (GCMs) is essential. Due to their sub-grid scale, internal variability, and boundary layer interactions, trade wind cumulus clouds are not well represented in NWP and GCMs (Kollias and Albrecht, 2010). An important source of uncertainty of these models is caused by an insufficient representation of the first aerosol effect (Bony and Dufresne, 2005), which describes the correlation of the cloud droplet number concentration N and the cloud optical thickness τ or cloud top reflectivity $\mathcal{R}$, commonly known as the Twomey effect (Twomey, 1977). It is most prominent for optically thin, low-level clouds such as trade wind cumulus (Platnick and Twomey, 1994; Werner et al., 2014), which are an ubiquitous cloud type in the tropics (Warren et al., 1988; Eastman et al., 2011). Despite their small vertical and horizontal extent, trade wind cumuli can have fractional cloudiness of more than $25\,\%$ (Albrecht, 1991) and, therefore, may influence the Earth radiative energy budget significantly (Chertock et al., 1993). In addition, trade wind cumuli play an important role in maintaining the thermodynamic energy budget in the atmospheric boundary layer. They couple the surface and free atmosphere by transporting latent heat and developing deep convection (Lamer et al., 2015). Another important factor determining the CRF is the number concentration of aerosol particles, in particular the amount of particles which can act as cloud condensation nuclei (CCN) (Werner et al., 2013). Depending on the CCN number concentration, precipitation formation can be promoted or inhibited (Lee and Feingold, 2013). The CCN concentration influences the cloud life cycle and life time (Albrecht, 1989). The magnitude of both effects depends on the individual cloud regime.

Operational NWP models usually do not have the computational capability to consider size-resolved microphysical schemes and, therefore, the usage of simplified parametrizations is inevitable. The most important parameter, which links microphysical and radiative properties of clouds, is the cloud droplet effective radius r_{eff}, which represents the radiative effective size of a cloud droplet population (Pontikis and Hicks, 1992). In NWP and GCMs, r_{eff} is calculated from the cloud droplet number concentration N and the liquid water content LWC. In simple models, assumptions of constant N are applied for different situations, e.g., the classification of polluted and clean air-masses. As r_{eff} is derived from LWC and N, the cloud droplet number concentration is a key parameter for models to calculate reasonable values of r_{eff} and to represent the Twomey effect. Also for NWP with two-moment schemes, which use N in addition to the mass-mixing ratio, a validation of N as a prognostic variable emerges.

To measure N and LWC, airborne in-situ measurements are applied, utilizing different physical methods and instruments (Baumgardner et al., 2011; Wendisch and Brenguier, 2013). These are based on optical measurement principles such as for-

ward scattering, phase doppler interferometry, and holographic imaging. Beside the uncertainties of the individual measurement techniques, the total sample volume of the instruments is rather limited in comparison to the typical horizontal and vertical extent of clouds. Due to the limited flight time and range, airborne in-situ observations can not cover the natural variability of N, r_{eff}, and LWC completely. To directly quantify the Twomey effect, co-located measurements of cloud microphysical and radiative properties are required, which was realized only in a few occasions (Ackerman et al., 2000; Siebert et al., 2013; Werner et al., 2014).

To improve global statistics of estimates of the Twomey effect, several approaches to derive N from satellite observations have been developed (Grosvenor et al., 2018b; Quaas et al., 2009; Minnis et al., 2011; Mace et al., 2016; Bennartz and Rausch, 2017). These techniques provide useful global data sets with large spatial and temporal coverage. Based on passive remote sensing in the solar and terrestrial wavelength range, N is estimated combining the results of bi-spectral retrievals of cloud optical thickness τ and r_{eff}, and cloud top temperature T_{CT} by (Brenguier et al. (2000); Quaas et al. (2006); Zeng et al. (2014)). They assumed a vertically constant LWC and N throughout the cloud profile, which is at least for LWC not a realistic scenario. Slightly deviating, Bennartz and Rausch (2017) assumed a sub-adiabatic vertical profile where the LWC increases linearly with height with values corresponding to about $80\,\%$ of the respective adiabatic value. More complex vertical profile types of LWC and N are applied by Boers et al. (2006), where a heterogeneous mixing model assumes that entrainment dilutes the air parcel with constant mean-volume radius of the droplets r_{vol} (radius of those cloud droplets with a volume corresponding to the average of the volume size distribution of the cloud population), while r_{eff} follows an adiabatic profile. The retrieved values of N using the homogeneous or the heterogeneous model differ by several percent. Further studies show that the heterogeneous model represents nature more realistically compared to the homogeneous assumption (Boers et al., 1998; Brenguier et al., 2000). These methods often use the dependence of τ on N to connect cloud microphysical and radiative properties. However, so far no operational satellite products of N are available. Retrievals of N, in general, can have uncertainties of up to $80\,\%$ (Grosvenor et al., 2018b).

Assuming an adiabatic cloud, the LWC increases linearly with height and the liquid water path LWP is determined by integrating LWC from cloud base (CB) to cloud top (CT):

$$LWP = \int_{\mathrm{CB}}^{\mathrm{CT}} LWC(z)\,\mathrm{d}z = \frac{4}{3} \cdot \pi \cdot \rho_{\mathrm{w}} \cdot \int_{\mathrm{CB}}^{\mathrm{CT}} N(z) \cdot r_{\mathrm{vol}}^3(z)\,\mathrm{d}z \tag{1}$$

with the density of liquid water ρ_{w}, the geometric height z, and the mean-volume radius r_{vol}. Following Hansen and Travis (1974) and Stephens (1978) the cloud optical thickness τ is related to the LWP by:

$$\tau = \int_{\mathrm{CB}}^{\mathrm{CT}} \sigma_{\mathrm{ext}}\,\mathrm{d}z = \int_{\mathrm{CB}}^{\mathrm{CT}} \pi \int_0^\infty Q_{\mathrm{ext}}(x) \cdot N(r,z) \cdot r^2\,\mathrm{d}r\,\mathrm{d}z = \int_{\mathrm{CB}}^{\mathrm{CT}} \pi \cdot Q_{\mathrm{ext}}(\overline{x}) \cdot N(z) \cdot r_{\mathrm{srf}}^2\,\mathrm{d}z \tag{2}$$

with the extinction coefficient σ_{ext}, the extinction efficiency factor Q_{ext} which is approximately 2 for cloud droplets in the solar wavelength range, the size parameter $x = (2 \cdot \pi \cdot r)/\lambda$, and the mean radius r_{srf} (radius of those cloud droplets with a surface area corresponding to the average of the surface area size distribution of the cloud population). According to Martin et al.

(1994), the cloud droplet effective radius r_{eff} correlates with the mean-surface radius r_{srf} and the mean-volume radius r_{vol} of the droplet size distribution given by:

$$k = \left(\frac{r_{\text{vol}}}{r_{\text{eff}}}\right)^3 = \left(\frac{r_{\text{srf}}^3}{r_{\text{vol}}^2}\right)^6.$$ (3)

This relation depends on the shape of the droplet size distribution and is referred as the k-parameter (Martin et al., 1994). Using k as the distribution shape factor, r_{srf} and r_{vol} in Eq. (1) and Eq. (2) are replaced by r_{eff} leading to:

$$\tau = \frac{3 \cdot \int_{\text{h}_{\text{CB}}}^{\text{h}_{\text{CT}}} LWC(z) \cdot \text{d}z}{2 \cdot \rho_{\text{w}} \cdot r_{\text{eff}}}.$$ (4)

A typical value for the k-parameter in case of maritime clouds is $k = 0.8$ (Martin et al., 1994). Equation (4) assumes a homogeneous, adiabatic cloud characterized by a linear increase of LWC with height, which is not confirm with most cloud observations which showed that a majority of clouds are sub-adiabatic (Brenguier et al., 2000; Painemal and Zuidema, 2011; Min et al., 2012).

Instead of using τ in the retrieval of N, LWP from passive microwave sensors can be exploited (Minnis et al., 2011). This approach has the advantage that LWP is determined at wavelengths, which are not influence by aerosol particles, sun-glint, or three-dimensional (3D) radiative effects. Further on, active remote sensing techniques have been applied to derive N, e.g., by Austin and Stephens (2001) and Mace et al. (2016), who combined r_{eff} vertical profiles derived from cloud radar observations and τ obtained from passive solar remote sensing. Nevertheless, a disadvantage of the radar is that the radar reflectivity Z is mainly determined by large cloud droplets, which biases the results.

The dependence of τ on N is investigated by Quaas et al. (2009) using satellite measurements. The correlations of τ and N, obtained by satellite are weaker compared to aircraft remote sensing results or in-situ measurements, which is primarily due to the large-scale averaging of the satellite measurement (McComiskey and Feingold, 2008). Analyzing satellite measurements of large-scale averaged N and τ in different thermodynamic conditions and, therefore, varying LWP, updraft velocity and aerosol particle concentrations, mask the effect of N on τ. As a result, parameterizations derived from satellite observations are not well suited for trade wind cumuli with their highly variable and small-extent.

Airborne remote sensing techniques are able to bridge the scale gap between in-situ and satellite measurements, as they allow to sample individual clouds under specific conditions and to cover a sufficiently large area to quantify the natural variability of N, r_{eff}, and LWC.

Here, a method is proposed to combine passive and active airborne remote sensing measurements of cloud vertical profiles of microphysical parameters and cloud radiative properties. Measurements of upward radiance $I_\lambda^\uparrow$ collected by the Spectral Modular Airborne Radiation measurement sysTem (SMART) are used to determine τ, r_{eff}, and the thermodynamic phase of cloud water close to the cloud top. Observations by the High Altitude and LOng range research aircraft Microwave Package (HAMP), which comprises of a multi-channel microwave radiometer and a cloud radar, provide LWP and radar reflectivity profiles which are used to determine the cloud boundaries and allowing to discriminate between precipitating and non-precipitating clouds. Furthermore, an alternative retrieval to determine r_{eff} from the spectrometer-microwave combination of SMART and

HAMP is developed and tested. Lidar measurements by the Water Vapour Lidar Experiment in Space (WALES) are additionally implemented to determine the cloud top height h_{CT}, while HAMP and dropsondes provide estimates of the cloud base height h_{CB}.

This paper is structured as follows. In Section 2 the sensitivity of the cloud top reflectivity $\mathcal{R}$ (ratio of the upward radiance and downward irradiance) and cloud top albedo α (ratio of the upward and downward irradiance) of typical trade wind cumuli with respect to changes of N is quantified. To access the required accuracy of N retrievals and the cloud regime most sensitive to N. The remote sensing instruments utilized in this study are introduced briefly in Section 3. In Section 4 the retrieval of the optical properties and the cloud filtering is described. Subsequently, three different methods to determine N are presented in Section 5 and applied to synthetic measurements and two exemplary cases of trade wind cumulus. Resulting values of N are correlated with measured $\mathcal{R}$, separated for different thermodynamic conditions (binned LWP), to show the possibility to obtain parameterizations for the Twomey effect.
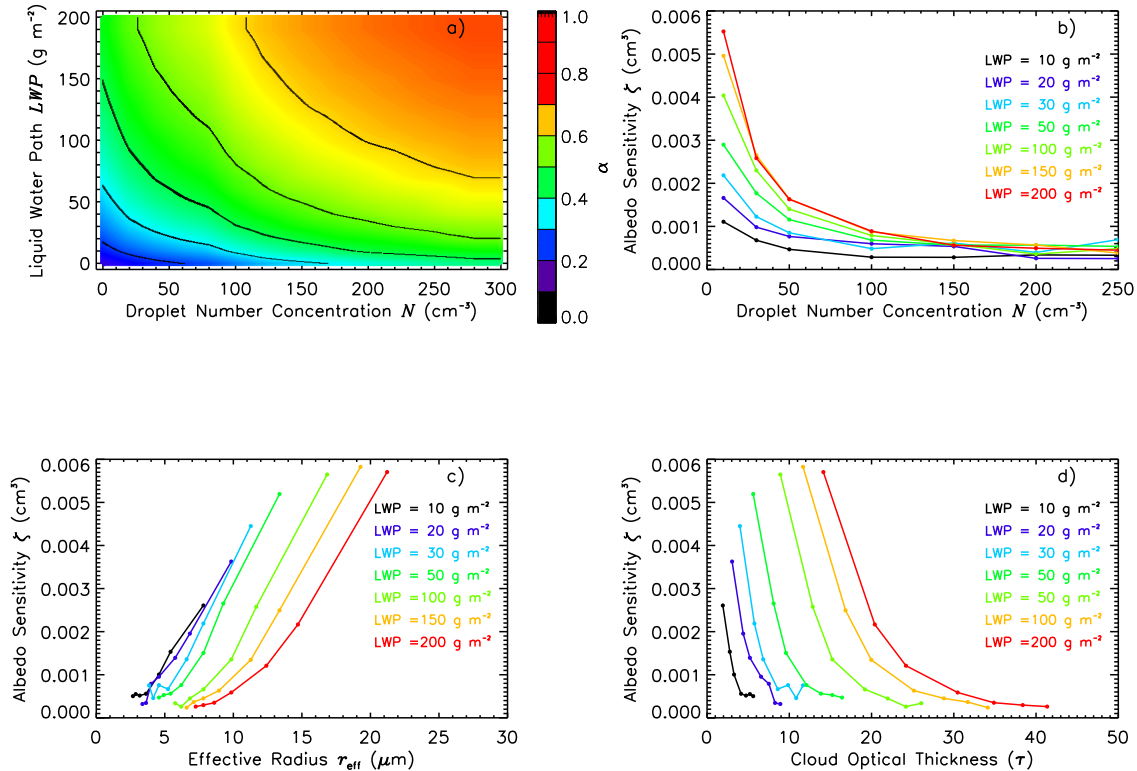
Figure 1. Simulations for a liquid water cloud between 1000 m and 1500 m with liquid water path LWP from $10\,\mathrm{g\,m^{-2}}$ to $200\,\mathrm{g\,m^{-2}}$ and for a solar zenith angle ϑ of $5°$. The simulations are integrated over a wavelength range from 250 nm to 2500 nm. Panel a) shows cloud top albedo α for combinations of the cloud droplet number concentration N and LWP. Panel b) shows cloud top albedo sensitivity ζ as a function of N for different LWP. Panel c) and d) display ζ as a function of effective radius r_eff and cloud optical thickness τ, respectively.

2   Sensitivity of the Twomey Effect for Different Cloud Regimes

To quantify the Twomey effect for trade wind cumulus with different LWP, radiative transfer simulations (RTS) with the radiative transfer package libRadtran 2.0.2 (Emde et al., 2016) are performed. The solar cloud top albedo was calculated for a homogeneous liquid water cloud located between 1000 m and 1500 m and a solar zenith angle ϑ of $5°$. Liquid water path is varied in a range between $10\,\mathrm{g\,m^{-2}}$ and $200\,\mathrm{g\,m^{-2}}$, typical for shallow trade wind cumulus (Siebert et al., 2013).

Figure 1a shows simulated α as a function of N and LWP. For constant LWP and increasing N (decreasing r_eff), α increases which is described by the Twomey effect. However, this sensitivity is not equal for the different LWP. For constant N and increasing LWP (increasing r_eff), α increases with different rates for N. This illustrates that different cloud regimes excerpt various sensitivities in terms of the Twomey effect. Therefore, LWP, N, and r_eff have to be considered to parameterize the

radiative properties of trade wind cumuli.

To quantify the Twomey effect for different cloud regimes, the cloud albedo sensitivity ζ is defined as:

$$\zeta(LWP, r_{\text{eff}}, N) = \frac{\mathrm{d}\alpha(LWP, r_{\text{eff}}, N)}{\mathrm{d}N}, \tag{5}$$

which represents the change of α with respect to an increase of N and is given in units of cm^3.

5 Figure 1b displays ζ as a function of N for different LWP. In general, ζ decreases with increasing N. Clouds with low LWP (black) and low N have a lower ζ compared to clouds with higher LWP (red) but same N. The highest ζ is obtained for clouds with the highest LWP of $200\,\text{g}\,\text{m}^{-2}$, while thicker clouds with the lowest LWP of $10\,\text{g}\,\text{m}^{-2}$ have the lowest ζ. Because of $r_{\text{vol}} \propto \sqrt[3]{LWP/N}$ the change of N for constant LWP is larger for large LWP (e.g. $200\,\text{g}\,\text{m}^{-2}$) compared to lower values of $LWP = 10\,\text{g}\,\text{m}^{-2}$ and resulting absolute differences in simulated α and ζ.

10 In Fig. 1c the cloud albedo sensitivity ζ is shown as a function of r_{eff} for clouds of different LWP. With cloud geometric thickness H and assuming a constant LWP, the effective radius determines N or vice versa following:

$$r_{\text{eff}} = \sqrt[3]{\frac{3 \cdot LWP}{4 \cdot \rho_{\text{w}} \cdot \pi \cdot H \cdot N} \cdot k^{-3}}. \tag{6}$$

For all LWP cases the sensitivity increases with increasing r_{eff} (decreasing N). This agrees with Fig. 1b where low N have the highest ζ. Clouds with lower LWP show higher ζ and, therefore are more sensitive to changes of r_{eff} compared to clouds
15 with higher LWP.

In Fig. 1d ζ is plotted as a function of τ, which is calculated using Eq. (4) from LWP, N, and r_{eff} used in the simulations. For all clouds with different values of LWP, ζ decreases with increasing τ. This implies that changes in N have larger effects on α for clouds with low τ. As a result, optically thin clouds with low N and large r_{eff}, which is the typical character of shallow trade wind cumulus, are subject to the strongest Twomey effect. Therefore, the Twomey effect of trade wind cumulus is highly
20 relevant for NWP and GCMs.

The simulations further illustrate the challenge of estimating α of shallow trade wind cumuli by satellite remote sensing. Typically, satellite retrievals of N can have uncertainties in the range of up to $80\,\%$ (Grosvenor et al., 2018b). For clouds with low N, e.g., $30\,\text{cm}^{-3}$ and $LWC = 0.1\,\text{g}\,\text{m}^{-3}$, the concentration of N might be biased by up to $\pm 23\,\text{cm}^{-3}$. This would result in a bias of α of ± 0.08 ($80\,\text{W}\,\text{m}^{-2}$ increased cloud forcing for $1000\,\text{W}\,\text{m}^{-2}$ insolation). For clouds with higher N of $200\,\text{cm}^{-3}$
25 the retrieval uncertainties of N increase in absolute terms ($\Delta N = \pm 156\,\text{cm}^{-3}$) and lead to a similar uncertainty of $\alpha = \pm 0.07$ even though ζ is reduced for clouds with higher N. This shows, that retrievals of N need to be improved, in order to reduce the uncertainties of global estimates of N and α calculations in NWP and GCM.

3 Observations and Instrumentation

Convective low-level cumuli have been observed by airborne remote sensing during the second Next Generation Remote Sens-
30 ing for Validation Studies (NARVAL-II) campaign between 8 and 31 August 2016 (Stevens et al., 2018). The High Altitude and Long Range Research Aircraft (HALO) based on Barbados was mostly flying eastward into an area dominated by shallow

Table 1. Measured and retrieved quantities from SMART, HAMP, WALES, and the dropsondes.

Instrument	Measured / retrieved quantity	Variable	Unit
SMART	Upward radiance	$I_\lambda^\uparrow$	$\mathrm{W\,m^{-2}\,sr^{-2}}$
	Cloud optical thickness	τ	-
	Effective radius	r_{eff}	$\mu\mathrm{m}$
	Liquid water path	LWP_{A}	$\mathrm{g\,m^{-2}}$
HAMP	Liquid water path	LWP_{B}	$\mathrm{g\,m^{-2}}$
	Radar reflectivity	Z	dBz
WALES	Cloud top height	h_{CT}	m
Dropsondes	Temperature	T	$^\circ$C
	Dew-point temperature	T_{d}	$^\circ$C
	Lifting condensation level	h_{LCL}	m

trade wind cumulus unaffected by anthropogenic influences. HALO was equipped with a set of passive and active remote sensing instruments. Reflected solar radiation was measured by the passive instruments SMART (Wendisch et al., 2001, 2016) and specMACS (Ewald et al., 2016), while radiation emitted in the microwave spectral range was measured by the HALO Microwave Package (HAMP). For active remote sensing, HAMP included a cloud radar (Mech et al., 2014). Lidar observations by the WAter vapor Lidar Experiment in Space (WALES) completed the cloud remote sensing instrumentation. WALES measures the backscatter coefficient and depolarization at 532 nm and 1064 nm wavelength, and contains a high spectral resolution lidar channel at 532 nm wavelength (Wirth et al., 2009). Additionally, numerous dropsondes were released from HALO.

All instruments were pointed into nadir direction and synchronized in time. However, the different Field-of-Views (FOV) of the instruments cause a systematic difference in the observed time series. All measured and retrieved quantities from SMART, HAMP, WALES, and the dropsondes are summarized in Table 1.

3.1 Spectral Modular Airborne Radiation measurement sysTem

During NARVAL-II, SMART measured the spectral upward $F_\lambda^\uparrow$ and downward irradiance $F_\lambda^\downarrow$, as well as spectral upward radiance $I_\lambda^\uparrow$. Each quantity was recorded with two separate Zeiss grating spectrometers, one for the visible (VIS) range from 300 nm to 1000 nm wavelength and a second one for sampling the near-infrared (NIR) range from 900 nm to 2200 nm. By merging the spectra, about 97 % of the solar spectrum is covered (Bierwirth et al., 2009). The spectral resolution defined by the full width at half maximum is 2 - 3 nm for the VIS spectrometer and 8 - 10 nm for the NIR spectrometer.

The radiance optical inlet of SMART has an opening angle of 2°. The sampling time t_{int} was set to 0.5 s. For an average aircraft ground-speed of about $220\,\mathrm{m\,s^{-1}}$ and a distance of 10 km between cloud top and the aircraft this results in a FOV of about 100 m x 120 m for an individual pixel.

The optical inlets for $F_\lambda^\uparrow$ and $F_\lambda^\downarrow$ mainly consist of integrating spheres, which collect direct and scatter solar radiation from the

upper or lower hemisphere. During NARVAL-II, the upward-looking inlet was equipped with an active stabilization platform to ensure horizontal alignment of the sensor, which is crucial as $F_\lambda^\downarrow$ refers to a horizontal plane (Wendisch et al., 2001).

Prior and after NARVAL-II, SMART was radiometrically calibrated in the laboratory using certified calibration standards traceable to the National Institute of Standards and Technology (NIST). A secondary calibration by a mobile standard was applied during the campaigns to track potential changes of the instrument sensitivity. The total measurement uncertainty of downward irradiance $F_\lambda^\downarrow$ and upward radiance $I_\lambda^\uparrow$ for typical conditions and observations of shallow cumulus is about 5.4% for the VIS and 8.4% for the NIR range, which is composed of individual errors due to the spectral calibration, the spectrometer noise and dark current, the primary radiometric calibration (Brückner et al., 2014).

3.2   HALO Microwave Package

HAMP is a combination of a passive microwave radiometer and an active cloud radar specifically designed for the operation on HALO (Mech et al., 2014). The microwave radiometer includes 26 frequency channels between 22.24 GHz and 183.31 GHz $\pm$ 12.5 GHz. The brightness temperature (BT) measured along the 22.24 GHz and 183.31 GHz rotational water vapor lines provide the total column water vapor (Schnitt et al., 2017) and information on its vertical distribution. Liquid water emission increases roughly with the frequency squared. By combining BT in window channels, i.e., 31.4 GHz and 90 GHz, mostly affected by liquid water with channels sensitive to water vapor, the LWP can be retrieved. This principle is also employed by satellite instruments which provide global climatologies of LWP, but suffer from the coarse footprint of a few 10ths of kilometer (Elsaesser et al., 2017).

The statistical LWP retrieval is based on a large variety of atmospheric profiles with differently structured warm clouds as training data composed from the dropsondes (Schnitt et al., 2017). Synthetic BT are simulated from these profiles and subsequently used to fit a multi-parameter linear regression model employing higher order terms (Mech et al., 2007). Testing the retrieval algorithm on an independent sub-sample provides an accuracy of about $20\,\mathrm{g\,m^{-2}}$ for LWP values below $100\,\mathrm{g\,m^{-2}}$ and an accuracy of 20% for LWP above (Jacob et al., 2019).

The cloud radar MIRA-36 operates at a frequency of 36 GHz and has a similar horizontal resolution as the LWP of about 1000 m and a temporal resolution of 1 s. Vertical profiles are divided into 30 m bins (Mech et al., 2014). The radar provides different parameters linked to the cloud microphysical properties including the radar reflectivity Z, the linear depolarization, and the Doppler velocity and the spectral width of the droplet size distribution. Note, that the latter two are affected by the relative motion of the aircraft to the wind and the antenna width (Mech et al., 2014).

Radar reflectivity represents the sixth moment of the cloud droplet size distribution and, therefore, is strongly influenced by large droplets. In order to calculate the LWC, which is proportional to the third moment of the droplet size distribution (DSD), from Z so-called $Z - LWC$ relations are used, which are typically derived from in-situ measurements. According to Khain et al. (2008), there is quite some variability involved and as soon as the transition to drizzle sets in the relation can be off by orders of magnitude. Here the $Z - LWC$ relation

$$LWC_\mathrm{p} = LWP \cdot \frac{\sqrt{Z_\mathrm{p}}}{\sum_{j=1}^{j=M} \sqrt{Z_j} \cdot \Delta h} \tag{7}$$

following Frisch et al. (2000) is used to derive vertical profiles of LWC. With the binned LWC_p at height gate p resulting from the vertical resolution of the radar, the LWP of the cloud, is distributed by the weighting of Z_p (Z at height gate p) and $\sum_{j=1}^{j=M} \sqrt{Z_j}\Delta h$ the sum of the Z, over all height gates where a cloud was present. The techniques to derive brightness temperatures and radar reflectivity profiles are described in more detail by Konow et al. (2018).

3.3 Water Vapour Lidar Experiment in Space (WALES)

The DIfferential Absoption Lidar (DIAL) called WALES operates at four wavelengths near 935 nm to measure atmospheric water vapor. Mixing ratio profiles covering the whole atmosphere below the aircraft. WALES also contains channels for aerosol measurements at 532 nm and 1064 nm wavelength with depolarization detection. At 532 nm, WALES uses the high-spectral
10 resolution technique, which distinguishes molecular from particle backscatter, to enable direct extinction measurements. Within this study only the aerosol channels are used to provide information on the cloud top height. The ranging resolution of the instrument is 15 m. Together with the flight altitude inferred from the HALO on-board positioning system and an appropriate attitude correction the accuracy of the cloud top height detection is about 20 m.
The laser has a beam divergence of 1 mrad, which leads to an illuminated spot of 10 m diameter on ground at a flight altitude
15 of 10 km. Laser pulses are emitted with a repetition rate of 100 Hz. 20 signals are averaged to improve the signal to noise ratio, resulting in an along flight track resolution of 44 m at $200\ \mathrm{m\,s^{-1}}$ aircraft speed. Thus, the horizontal resolution is reduced as compared to SMART and HAMP. Along track, this can be taken into account by further signal averaging.

4 Measurement Analysis

Trade wind cumuli mostly appear randomly distributed with a tendency to form self-organizing structures (Bony et al., 2015).
20 Typically, the vertical cloud extent is larger than the horizontal one within an individual cell. This is in contrast to stratiform cloud fields if common retrieval techniques to derive N are applied. Clouds smaller than pixel size covered by the FOV, bias the retrieval of the microphysical properties (Oreopoulos and Davies, 1998a, b). The dominance of small-scale cumulus during NARVAL-II, ranging in the horizontal size of a few hundred meters, results in heterogeneous cloud scenes. This induces challenges with respect to cloud masking and RTS.

4.1 Cloud Mask and Precipitation Flag

4.1.1 Cloud Mask

To distinguish between cloud and cloud-free measurements over ocean surfaces, the difference in the spectral reflectivity is analyzed. The ratio χ of $I_\lambda^\uparrow$ between 858 nm and 648 nm wavelength is calculated in analogy to the MODIS cloud mask

(Platnick et al., 2013) by:

$$\chi = \frac{I^{\uparrow}_{858}}{I^{\uparrow}_{648}}. \tag{8}$$

The cloud mask is based on the relative intensity of $I^{\uparrow}_{\lambda}$ and χ. Therefore, a single measurement can be identified as cloudy when only a part of the SMART FOV with 100 m x 120 m is cloud covered. Masking each measurement point as cloudy or cloud-free, the cloud length l_{cld} is determined, by counting the number n of consecutive cloud masked measurements. Multiplied with the flight speed v_{ac} and the constant integration time of SMART of $t_{\mathrm{int}} = 0.5$ s, the cloud length is calculated by:

$$l_{\mathrm{cld}} = n \cdot t_{\mathrm{int}} \cdot v_{\mathrm{ac}}. \tag{9}$$

For $v_{\mathrm{ac}} \approx 220 \, \mathrm{m \, s}^{-1}$ the smallest resolvable cloud size is in the range of 120 m along flight track.

The length of trade wind cumulus can be shorter than the SMART FOV. To identify such cases, an additional homogeneity cloud flag (HCF) is introduced. The cloud is considered homogeneous (HCF is true) when a single observation is enclosed by 5 cloud masked measurements. For clouds not surrounded by at least two cloudy pixel, the HCF is set to false. Therefore, the HCF identifies clouds that are large enough to fill the FOVs of SMART, HAMP, and WALES at the same time.

4.1.2 Precipitation Flag

Precipitation is identified using the radar reflectivity Z. Measurements are considered to be affected by precipitation when Z exceeds a threshold of $Z <$ -20 dBz within 50 m to 200 m above sea level (Schnitt et al., 2017). This allows to discriminate precipitation events, which affect the LWP measured by the microwave radiometer and retrieved by SMART. The simple thresholding of radar reflectivity close to the sea surface does might not capture all precipitating clouds as drizzle particles might evaporate before reaching the lower 200 m close to the sea surface.

4.2 Retrieval of Cloud Optical Thickness and Droplet Effective Radius

Based on the reflected solar radiance $I^{\uparrow}_{\lambda}$ measured by SMART, a retrieval of τ and r_{eff} is performed, applying the radiance ratio method proposed by Werner et al. (2013). The use of radiance ratios at two different wavelength reduces the uncertainties by the radiometric calibration of SMART. For the wavelength ratio applied here, an uncertainty of $6\,\%$ is assumed. Additionally, the use of ratios increases the retrieval sensitivity with respect to r_{eff} by clearly separating the dependence of $I^{\uparrow}_{\lambda}$ on τ and r_{eff} and, therefore, the retrieval accuracy. Forward simulations of reflected spectral radiance $I^{\uparrow}_{\lambda}$ were carried out with the libRadtran 2.0.2 package (Emde et al., 2016). The Fortran 77 discrete ordinate radiative transfer solver version 2.0 (FDISORT 2) after Stamnes et al. (2000) is used. The extraterrestrial $F^{\downarrow}_{\lambda}$ is given by Gueymard (2004) and a marine aerosol profile after Shettle (1989) is selected. Vertical profiles of air temperature, pressure, and humidity are obtained from radiosonds released at the Bridgetown International Airport. For the optical properties of liquid water droplets, Mie calculations are performed.

The optical thickness τ and r_eff are determined by a modified Look-Up-Table (LUT) method after Nakajima and King (1990). While τ is derived at 870 nm wavelength, r_eff is retrieved with the radiance ratio method, using a ratio of measurements at 1050 nm and 1645 nm wavelength. Compared to retrievals using larger wavelength, e.g., 2.1 or 3.7 μm, r_eff retrieved by the SMART measurements does not only represent the cloud particles at cloud top. The vertical weighting function for 1.6 μm covers significant amount of information from lower cloud layers (Platnick, 2000). Therefore, retrieved r_eff are smaller than the actual cloud droplet size at CT which are considered in Eq. (12) to calculate N. This leads to a systematic overestimation of N calculated from SMART measurements. Results from the SMART optical properties retrieval are denoted with subscript "A".

Clouds, which do not cover the entire FOV of SMART, bias the retrieved optical properties, because they violate the assumption of plane parallel clouds used in the RTS (Oreopoulos and Davies, 1998a, b). Lower values of $I_\lambda^\uparrow$ bias τ towards lower values, whereas r_eff is shifted to larger droplet sizes (Cahalan et al., 1995). Further on, the heterogeneous structure of trade wind cumulus is likely to cause 3D radiative effects, like shadowing cloud areas by nearby cloud-towers, or enhanced reflectivity due to additional reflection into the FOV. These effects may also bias the retrieval of τ and r_eff and the calculation of N. Therefore, the HCF filter is applied to exclude measurements that are influenced by these processes. However, due to the low vertical extent of shallow trade wind cumuli which are analyzed here, these 3D radiative effects are assumed to be negligible. Liquid water path is obtained directly from libRadtan on the basis of τ and r_eff similar to Eq. (4). Liquid water path derived from SMART is again denoted with subscript "A". In case of cloud heterogeneity, sun-glint, or 3D radiative effects, the retrieval of τ is very likely biased. Following Eq. (4), a bias of τ also influences the retrieval of r_eff and, therefore, LWP. To mitigate these effects, measurements of LWP from HAMP (denoted with subscript "B") are applied in the libRadtran radiation simulations of the cloud retrieval. Liquid water path data from microwave radiometers are obtained from wavelengths not influenced by sun-glint or 3D radiative effects. Using LWP from HAMP as a precondition, the LUTs reduce to one absorbing wavelength sensitive to r_eff. Therefore, the non-linear dependence between τ and r_eff is removed and the retrieval becomes more reliable. Retrieved r_eff from combined passive solar radiance and microwave measurements are denoted with subscript "B".

5   Retrieval of Cloud Droplet Number Concentration

The retrieval of N from remote sensing observations is based on the relation proposed by Brenguier et al. (2000) and Wood (2006), which links N of a stratiform cloud to τ and r_eff by:

$$N_\text{A} = \frac{\sqrt{10}}{4 \cdot \pi \cdot \sqrt{\rho_\text{w}}} \cdot \sqrt{f_\text{ad} \cdot \Gamma_\text{ad}} \cdot \frac{\sqrt{\tau}}{\sqrt{r_\text{eff,A}^5}}. \tag{10}$$

The technique assumes an adiabatic vertical cloud profile, where temperature linearly decreases and LWC linearly increases with height. An adiabatic profile implies that the total water mass mixing ratio of the cloud is conserved. This is true when: (i) no water is removed from the cloud (no precipitation or fallout), (ii) no entrainment of dryer air at the cloud edges occurs, and (iii) no evaporation from precipitation happens. As a result, the proposed method should be applied to non-precipitating clouds only, which do not undergo strong vertical convection and mixing. A vertically constant N throughout the cloud layer

Table 2. Overview of the cloud droplet number concentration retrievals and applied measurements, retrieval parameters, and assumptions.

Method	A	B	C
Instruments and Parameters			
SMART	$\tau, r_{\mathrm{reff,A}}$	$r_{\mathrm{reff,B}}$	$r_{\mathrm{reff,B}}$
HAMP	$\times$	LWP	LWP
WALES	$\times$	$\times$	f_{calc}
Assumptions			
adiabatic cloud-profile	✓	✓	$\times$
adiabatic change of LWC	$f_{\mathrm{ad}} \cdot \Gamma_{\mathrm{ad}} = 2.5 \cdot 10^{-3}\,\mathrm{g\,m^{-3}\,m^{-1}}$		Γ_{calc}
k-parameter	$k = 0.8$	$k = 0.8$	$k = 0.8$
const. N	✓	✓	✓
deep convection	$\times$	$\times$	$\times$
cloud homogeniety	✓	✓	✓
precipitation	$\times$	$\times$	$\times$
min. hori. size	$\approx 150\,\mathrm{m}$	$\approx 150\,\mathrm{m}$	$\approx 150\,\mathrm{m}$

is assumed. This assumption is verified for stratiform clouds and shallow trade wind cumulus by in-situ measurements, e.g., Reid et al. (1999) and Wendisch and Keil (1999). The vertically constant N is mainly determined by the amount of available CCN at cloud base and their potential to form cloud droplets depending on the degree of supersaturation, which is controlled by temperature, entrainment of dry air, and updraft velocity.

5 The k-parameter, relating the effective radius r_{eff} and the volumetric radius r_{vol}, is set to $k = 0.8$ for marine clouds following the suggestion by Martin et al. (1994) and Pontikis (1996). Depending on the cloud type the k-parameter can vary by ± 0.1 (Martin et al., 1994).

With help of cloud properties retrieved by airborne remote sensing Eq. (10) can be applied in different complexity to derive N. In the following three methods are proposed. Method A uses only SMART data, while method B additionally includes HAMP

10 observations of LWP, whereas method C also involves measurements by WALES. The obtained parameters and applied assumptions are summarized in Table 2.

5.1 Method A: Based on Cloud Optical Thickness and Droplet Effective Radius

Method A follows the traditional satellite approach to feed Eq. (10) with τ and r_{eff} obtained by a single passive remote sensing

15 instrument. Here, τ_{A} and $r_{\mathrm{reff,A}}$ retrieved by SMART are applied. Using the radiance ratio retrieval of SMART to derive τ and $r_{\mathrm{eff,A}}$ from two infrared wavelengths, absolute calibration errors are reduced and the sensitivity on r_{eff} is increased. The degree of adiabacity is assumed to be 1. This implies, that for trade wind cumuli, which are typically sub-adiabatic, the estimated N is

potentially biased. However, similar retrieval assumptions are frequently applied to observations from satellite such as MODIS (Grosvenor et al., 2018b).

5.2 Method B: Based on Liquid Water Path and Droplet Effective Radius

For adiabatic clouds, Eq. (4) can be solved analytically, which results in a relation that directly links LWP to τ and r_{eff}:

5 $$LWP = \frac{5}{9} \cdot \rho_{\mathrm{w}} \cdot \tau \cdot r_{\mathrm{eff}} \tag{11}$$

following (Brenguier et al., 2000). Equation (11) allows to apply Eq. (10) with an independent measure of LWP instead of τ to calculate N. As given by Wood (2006) combining Eq. (10) and Eq. (11) leads to:

$$N_{\mathrm{B}} = \frac{3 \cdot \sqrt{2}}{4 \cdot \pi \cdot \rho_{\mathrm{w}}} \cdot \sqrt{f_{\mathrm{ad}} \cdot \Gamma_{\mathrm{ad}}} \cdot \frac{\sqrt{LWP_{\mathrm{B}}}}{r_{\mathrm{eff,B}}^3}. \tag{12}$$

In method B, LWP measurements by HAMP and derived $r_{\mathrm{eff,B}}$ from the combined SMART microwave-radiometer retrieval
10 are applied. The results are denoted with N_{B}. Exchanging $r_{\mathrm{eff,A}}$ by $r_{\mathrm{eff,B}}$ takes into account that LWP is determined from HAMP only. This makes the retrieval independent of τ derived by SMART and, therefore, less sensitive to effects by sun glint. Further on, LWP determination from HAMP applies wavelengths between 20 and 100 GHz, which are not influenced by aerosol particles. An additional advantage of the determination of LWP from HAMP is the separation of clouds for different LWP and to untangle the effects of varying LWP on α (McComiskey and Feingold, 2008).

15 ## 5.3 Method C: Based on Liquid Water Path, Droplet Effective Radius, and Cloud Geometric Thickness

Equations (10) and (12) assume constant values of f_{ad} and Γ_{ad}. Therefore, in method A and B the adiabatic profile of LWC follows the maximum, theoretically possible profile under which liquid water is released due to condensation from upward motion in the atmosphere.

In-situ measurements of stratocumulus and trade wind cumulus indicate that a majority of cloud profiles do not follow this
20 adiabatic assumption (Wendisch and Keil, 1999; Merk et al., 2016). In most cases the profiles are sub-adiabatic, meaning a reduced increase of LWC with height, mostly due to entrainment and mixing from dry air at the cloud edges. When convection and mixing is moderate, an equilibrium between the droplets and the surrounding air can be assumed. Entrainment and mixing reduce f_{ad} but not necessarily N. Further it might reduce the (super-)saturation at the cloud edges causing a shrinking of the droplets but not their complete vanishing. To account for a sub-adiabatic increase of LWC with height in method C, $f_{\mathrm{ad}} \cdot \Gamma_{\mathrm{ad}}$
25 is replaced by observations. Observed Γ_{calc} is determined by:

$$\Gamma_{\mathrm{calc}} = \frac{2 \cdot LWP_{\mathrm{B}}}{H^2} \tag{13}$$

with LWP_{B} obtained by the microwave radiometer. The cloud geometric thickness $H = h_{\mathrm{CT}} - h_{\mathrm{LCL}}$ is estimated from a combination of the WALES cloud top height h_{CT} observations and h_{LCL} from dropsondes.

WALES can only derive h_{CT} when the laser is attenuated by clouds with high τ. As a result, the lidar signal is attenuated

soon and the cloud base height is not detectable. Therefore, $h_{CB} = h_{LCL}$ is determined separately from dropsondes, which represent the large-scale thermodynamic structure of the atmosphere. Using the temperature T and dew point temperature T_d at the two lower most points of the sounding, the lifting condensation level with $h_{LCL} \approx 125 \cdot (T - T_d)$ is approximated (Espy, 1836). Nevertheless, uncertainties of estimated h_{LCL} from dropsondes are in the range of ± 35 m not considering additional uncertainties caused by the assumptions in the equation (Romps, 2017). Alternatively, cloud boundary determination by combinations of lidar, radar, and dropsonde are applied, where: (i) the cloud droplets are large enough to produce a detectable radar echo and (ii) no precipitation is present, but are complicated for heterogeneous cloud fields. Selection of the appropriate instrument synergy depends on the observed cloud scene. Utilization of radar observations is preferred giving the best vertical resolution for well defined cloud edges. Using the estimated Γ_{calc}, Eq. (12) changes to:

$$N_C = \frac{3 \cdot \sqrt{2}}{4 \cdot \pi \cdot \rho_w} \cdot \frac{LWP_B}{H \cdot r_{eff,B}^3}. \tag{14}$$

5.4 Simulated Synthetic Measurements

To systematically test the potential of the proposed synergistic retrieval methods, synthetic measurements of spectral upward radiance $I_{\lambda,syn}^{\uparrow}$ are created. In that way, the three different methods are compared omitting the influence by measurement errors. Further on, varying environmental conditions, like sea surface albedo, heterogeneous cloud conditions, and 3D cloud radiative effects do not influence the systematic comparison of the retrieval methods. The comparison is based on retrieved cloud droplet number concentration N with methods A, B, and C and N_{cld} calculated from the model clouds serving as truth value.

Six synthetic clouds are simulated. Their respective parameters are listed in Table 3. Cloud droplet number concentrations N_{cld} of $50 \, \mathrm{cm}^{-3}$, $100 \, \mathrm{cm}^{-3}$, and $200 \, \mathrm{cm}^{-3}$ represent the typical range of pristine shallow trade wind cumulus (Siebert et al., 2013). For each N_{cld} an adiabatic and a sub-adiabatic cloud profile was set up. Cloud base height is 500 m and cloud top height is 1000 m. For all cloud cases a linear increase of LWC and a constant N_{cld} with height are assumed. In the adiabatic cases (I, III, V) a LWP of $362 \, \mathrm{g\,m}^{-2}$ and an adiabatic increase of LWC with height Γ_{ad} of $2.9 \cdot 10^{-6} \, \mathrm{kg\,m}^{-3} \mathrm{m}^{-1}$, for a surface temperature of $\approx 30°\,\mathrm{C}$ are used. For the sub-adiabatic cases (II, IV, VI) Γ is set to $\Gamma_{ad} \cdot 0.6 = 1.7 \cdot 10^{-6} \, \mathrm{kg\,m}^{-3} \mathrm{m}^{-1}$ representing a cloud which follows Γ_{ad} by 60% and leads to a LWP of $217 \, \mathrm{g\,m}^{-2}$. To calculate the volumetric radius $r_{vol}(z)$, the cloud profiles are divided into 20 layers of equal thickness of 25 m. For each layer the parameterization of Martin et al. (1994) is applied:

$$r_{vol}(z) = \sqrt[3]{\frac{3 \cdot LWC(z)}{4 \cdot \rho_w \cdot \pi \cdot N_{cld}}}. \tag{15}$$

In the radiative transfer model, the effective radius r_{eff} is used to determine the optical properties of the cloud particles instead of the volumetric radius r_{vol}. To convert $r_{vol}(z)$ into $r_{eff}(z)$ a k of 1.0 is applied, what considers the monodisperse droplet size distribution used in the model clouds. The synthetic measurements of $I_{\lambda,syn}^{\uparrow}$ are calculated with the same simulation set-up as for the cloud retrieval described in Section 4.2.

Simulated synthetic measurements of $I_{\lambda,syn}^{\uparrow}$ are applied to the retrieval method of τ, r_{eff}, and N of Section 5. All three methods A, B, and C are applied and results are denoted with additional subscript "R". The true values of τ from the RTS (subscript

"lib") are calculated directly from the given $r_{\mathrm{eff,lib}}$, which represents the cloud top r_{eff} of the model cloud. Total cloud optical thickness τ_{lib} and $r_{\mathrm{eff,lib}}$ from the libRadtran radiative transfer simulations are considered to be the reference values which are used to compare the retrieval results and the calculated N. For consistency the labeling of N for the three methods follows Section 5. An overview of all retrieved and calculated parameters is given in Table 3.

5   The retrieved cloud optical thickness τ_{R} is higher compared to the true value τ_{lib} for all cloud cases. The largest difference of 26% are observed for cloud I. With increasing N_{cld} the absolute and relative differences become smaller. Systematically larger errors are found for the adiabatic clouds. A similar pattern is obtained for $r_{\mathrm{eff,R}}$ which is always up to 2% smaller then $r_{\mathrm{eff,lib}}$. The sub-adiabatic clouds show the largest differences. The relative error decreases for higher N_{cld}. The systematic underestimation of $r_{\mathrm{eff,R}}$, especially for the sub-adiabatic cases, with respect to $r_{\mathrm{eff,lib}}$ results from the penetration depth of

10   the incident solar radiation into the cloud. For constant LWP, clouds with lower N have a lower τ, which reduces scattering. Therefore, the incident radiation can penetrate deeper into the cloud compared to clouds with higher N and τ (Platnick, 2000). As a result, $I_\lambda^\uparrow$ is more influenced by lower cloud layers and the retrieved $r_{\mathrm{eff,R}}$ is systematically smaller than $r_{\mathrm{eff,lib}}$. In this case, $r_{\mathrm{eff,R}}$ is not representing $r_{\mathrm{eff,lib}}$ at CT. The bias of $r_{\mathrm{eff,R}}$ from the $r_{\mathrm{eff,lib}}$ at CT feeds back into the retrieval of τ_{R} because of the dependence of τ and r_{eff} and the non-rectangular shape of the Look-Up-Table. The overall underestimation of

15   retrieved $r_{\mathrm{eff,R}}$, which appears for all passive remote sensing measurements based on reflected solar radiation, generally leads to an overestimation of N, which is intensively discussed, e.g., by Brenguier et al. (2000) and Grosvenor et al. (2018b, a) and therefore, not repeated here.

Liquid water path LWP_{R} is calculated with Eq. (11) from the retrieved τ_{R} and $r_{\mathrm{eff,R}}$ by assuming an adiabatic cloud profile. In all cases, the retrieval overestimates LWP_{R} by 18% for low N_{cld} up to 27%. The deviation becomes larger for high N_{cld}.

20   The cloud droplet number concentration $N_{\mathrm{A,lib}}$ is calculated with method A by using τ_{lib}, $r_{\mathrm{eff,lib}}$, and assuming an adiabatic vertical profile with Γ_{ad}. This provides a reference for $N_{A,R}$ which applies τ_{R} and $r_{\mathrm{eff,R}}$. By comparing $N_{\mathrm{A,lib}}$ and $N_{\mathrm{A,R}}$ the influence of the remote sensing retrieval method (forward simulations and error due to penetration depth) on N for different N_{cld} becomes obvious. In general, $N_{\mathrm{A,lib}}$ and $N_{\mathrm{A,R}}$ of all clouds are larger compared to N_{cld}. Differences between $N_{\mathrm{A,lib}}$, $N_{\mathrm{A,R}}$, and N_{cld} result from smaller retrieved $r_{\mathrm{eff,R}}$ and higher τ_{lib} compared to τ_{R}. Another reason is the difference between

25   Γ_{ad} used in the model cloud and the assumed LWP parameterization in Eq. (11) which is applied in Eq. (10) to correlate LWP and τ. For all clouds, $N_{\mathrm{A,R}}$ is larger then $N_{\mathrm{A,lib}}$ and N_{cld}, because in Eq. (10) N is dominated by $r_{\mathrm{eff}}^{-5/2}$ and less sensitive to $\tau^{1/2}$. Differences between $N_{\mathrm{A,lib}}$ and $N_{\mathrm{A,R}}$ vary between 0% and 17%, being largest for cloud I for which the deviation in $r_{\mathrm{eff,lib}}$ and $r_{\mathrm{eff,R}}$ is largest. The simulations also show that $N_{\mathrm{A,lib}}$ and $N_{\mathrm{A,R}}$ are largest for the sub-adiabatic cloud cases.

30   For method B, $N_{\mathrm{B,lib}}$ and $N_{\mathrm{B,R}}$ are larger then N_{cld} with smaller differences for the reference values of $N_{\mathrm{B,lib}}$ and larger differences of $N_{\mathrm{B,R}}$ compared to N_{cld}. For method B the deviations of $N_{\mathrm{B,lib}}$ and $N_{\mathrm{B,R}}$ compared to N_{cld} are largest for the sub-adiabatic cloud cases. The systematic overestimation of $N_{\mathrm{B,R}}$ for all clouds is due to the lower $r_{\mathrm{eff,R}}$. The differences reduce for increasing N_{cld} because the differences between $r_{\mathrm{eff,R}}$ and $r_{\mathrm{eff,lib}}$ decrease. This clearly shows that a wrong estimation of r_{eff} influences the calculation of N most significantly, while τ contributes to a minor part only, independently

35   which method is used. These results allow to conclude that r_{eff} must be retrieved close top. This is possible if the retrieval

Table 3. Overview of all six synthetic cloud cases. The predefined cloud liquid water path LWP and droplet number concentration N are denoted with subscript "cld". Cloud properties are calculated from the given cloud profile (subscript "lib") and retrieved from synthetic spectral cloud reflectivities (subscript "R"). Calculated N is listed for all three methods A, B, and C once using the predefined cloud properties "lib" and the retrieval results from "R".

	Cloud I adiabatic	Cloud II sub-adiabatic	Cloud III adiabatic	Cloud IV sub-adiabatic	Cloud V adiabatic	Cloud VI sub-adiabatic
N_{cld} [cm^{-3}]	50	50	100	100	200	200
LWP_{cld} [g m^{-2}]	362	217	362	217	362	217
τ_{lib}	35.6	25.5	45.2	32.3	57.3	41.0
$r_{\mathrm{eff,lib}}$ [μm]	18.8	18.8	14.9	12.6	11.8	10.0
τ_{R}	37.1	25.7	46.9	32.8	59.4	41.9
$r_{\mathrm{eff,R}}$ [μm]	18.3	15.4	14.8	12.3	11.9	9.9
LWP_{R} [g m^{-2}]	452	264	462	270	471	276
$N_{\mathrm{A,lib}}$ [cm^{-3}]	53	69	106	137	215	274
$N_{\mathrm{A,R}}$ [cm^{-3}]	58	74	111	145	215	288
$N_{\mathrm{B,lib}}$ [cm^{-3}]	52	68	105	134	211	268
$N_{\mathrm{B,R}}$ [cm^{-3}]	57	73	108	143	207	280
$N_{\mathrm{C,lib}}$ [cm^{-3}]	52	53	105	104	211	208
$N_{\mathrm{C,R}}$ [cm^{-3}]	57	57	108	111	207	217

applies appropriate wavelength in the infrared, where radiation is effectively absorbed within the upper most part of the cloud. Otherwise systematic overestimation of N occurs.

By applying method C the sub-adiabatic nature of the cloud profiles (II, IV, VI) is considered in the estimation of N. The calculated Γ_{calc} is assumed to be correct and identical to the profile of the constructed clouds, with $f_{\mathrm{ad}} = 0.6$ and $\Gamma_{\mathrm{calc}} = \Gamma_{\mathrm{ad}} \cdot 0.6$,

5   respectively. Therefore, it is obvious, that N calculated from method B and C are also identical for adiabatic clouds. In general, $N_{\mathrm{C,R}}$ derived from method C is closer to N_{cld} than $N_{\mathrm{B,R}}$. However, for the sub-adiabatic clouds (II, IV, VI) results for methods B and C differ. Cloud droplet number concentration $N_{\mathrm{C,lib}}$ is closest to N for all cloud cases and methods. The same pattern is present for $N_{\mathrm{C,R}}$ with the best agreement to N_{cld} compared to method A and B. Deviations in $N_{\mathrm{C,lib}}$ and $N_{\mathrm{C,R}}$ to N_{cld} are reduced with increasing N. This shows, that a correct assumption of Γ_{calc}, as possible with method C, is crucial for a reliable

10   calculation of N and can compensate biases in N which result from the the sub-adiabatic cloud profile.

5.5 Calculation of Retrieval Uncertainty of Cloud Droplet Number Concentration

Cloud droplet number concentrations calculated with Eq. (10), Eq. (12), and Eq. (14) are mainly effected by uncertainties from τ, LWP, and especially r_{eff}, but also depend on the accuracy of k, f_{ad}, and Γ_{ad}. To estimate the uncertainties of retrieved N, it is assumed that the errors are normally distributed and independent from each other. In this case the uncertainty of N_{A} from Eq. (10) is calculated by:

$$\Delta N = \sqrt{\left(\frac{\partial N}{\partial k}\right)^2 (\Delta k)^2 + \left(\frac{\partial N}{\partial f_{\mathrm{ad}}}\right)^2 (\Delta f_{\mathrm{ad}})^2 + \left(\frac{\partial N}{\partial \Gamma_{\mathrm{add}}}\right)^2 (\Delta \Gamma_{\mathrm{add}})^2 + \left(\frac{\partial N}{\partial \tau}\right)^2 (\Delta \tau)^2 + \left(\frac{\partial N}{\partial r_{\mathrm{eff}}}\right)^2 (\Delta r_{\mathrm{eff}})^2} \tag{16}$$

and analogous for Eq. (12) and Eq. (14). All uncertainties of N presented in the following sections are based on calculation by this approach. The uncertainties of the single parameters assumed in the calculations are summarized below.

For method A, B, and C, the uncertainty of k, representing the shape of the droplet size distribution, is set to $k = 0.8 \pm 0.1$ according to the range of values suggested by Martin et al. (1994) and Pontikis and Hicks (1992).

For methods A and B the degree of adiabiticity f_{ad} is fixed to one. In that case, no uncertainty in a measurement scene is attributed to f_{ad}. For method C, the uncertainty of f_{calc} is determined by the uncertainty of h_{CT}, h_{CB}, and retrieved LWP following Eq. (13). Cloud top height from WALES is determined with an accuracy of $\Delta h_{\mathrm{CT}} = \pm 20\,\mathrm{m}$. The cloud base height is derived from single dropsondes and, therefore, prone to horizontal variability of T, p, and T_{d}. Based on an analysis of different dropsondes in close vicinity, a cloud base height $h_{\mathrm{LCL}} = 660\,\mathrm{m} \pm 35\,\mathrm{m}$ is assumed. The evaluation of all dropsondes show that the thermodynamic conditions in the selected area stayed constant ($\Delta T < 2\,\mathrm{K}$ and $\Delta p < 4\,\mathrm{hPa}$) during the flight time with $h_{\mathrm{CT}} \approx 1800\,\mathrm{m}$, $T_{\mathrm{CT}} = 20.2°\mathrm{C}$, and $p_{\mathrm{CT}} = 820\,\mathrm{hPa}$. The accuracy of the deployed Vaisala dropsondes RD94 is reported to be within $\Delta T = \pm 0.2\,\mathrm{K}$ and $\Delta p = \pm 0.4\,\mathrm{hPa}$. Uncertainties of N_{C} caused by errors in Γ_{ad} are, therefore, negligible compared to the influence of τ and r_{eff}.

The adiabatic increase of LWC with height calculated from the Clausius-Clapeyron-Equation depends mostly on cloud top temperature T_{CT} and to a lower degree on cloud top pressure p_{CT}. Therefore, Γ_{ad} depends on T_{CT} and p_{CT}, too. The cloud droplet number concentration is mostly effected by the assumed T_{CT} whereby p_{CT} is only of minor contribution. Despite that, the cloud top pressure more strongly affects warm than cold clouds (Grosvenor et al., 2018b). For the uncertainty calculation, a temperature difference of 2 K is considered, which changes Γ_{ad} by $\pm 0.1 \cdot 10^{-3}\,\mathrm{g\,m^{-3}\,m^{-1}}$ for the reference value of $2.5 \cdot 10^{-3}\,\mathrm{g\,m^{-3}\,m^{-1}}$.

The uncertainty of the retrieval of τ and $r_{\mathrm{eff,A}}$ result from the measurements uncertainties of SMART which are described in Sec. 3.1. For typical trade wind cumulus uncertainties of ± 0.1 for τ and $\pm 1.1\,\mu\mathrm{m}$ for $r_{\mathrm{eff,A}}$ are assumed.

Small clouds not covering the entire FOV bias the retrieval of the optical properties towards low τ, large r_{eff} and resulting low N. Additionally, the uncertainties in r_{eff} increase for low τ. Correlation of τ and Δr_{eff} reveal, that this effect is pounced for $\tau \leq 5$. This mostly results from the increasing influence of the ocean surface with low albedo in broken cloud regions.

From the error estimation of the N retrieval it can be concluded that uncertainties in r_{eff}, LWP, and H have to be minimized as they influence the retrieval the most. Determination of h_{CB}, either from the dropsondes or the radar, and resulting H have to be accurate within at least $\pm 60\mathrm{m}$.

In addition to the measurement uncertainties, the sensitivities of the individual retrievals on τ, r_{eff}, LWP, h_{CT}, and h_{CB} have to be considered. It shows that the retrieval of LWP by SMART is sensitive for thin clouds (LWP $<100\,\mathrm{g\,m^{-2}}$) with an increasing uncertainty for optically thicker clouds caused by a reduced response of reflected $I^{\uparrow}$ in case of high optical thickness. The usage of LWP from SMART for optical thin clouds is further supported by the retrieval uncertainty in LWP by HAMP

5   for LWP values below $100\,\mathrm{g\,m^{-2}}$. For clouds with LWP around $100\,\mathrm{g\,m^{-2}}$ both methods A and B (assuming an uncertainty of LWP derived by HAMP of about $20\,\%$) lead to an uncertainty of N in the range of $10\,\mathrm{cm^{-3}}$. In case of thicker clouds ($LWP > 100\,\mathrm{g\,m^{-2}}$), method B with LWP from HAMP is used, achieving the N accuracy of $\pm 14\mathrm{cm^{-3}}$ from SMART. Clouds with $LWP > 100\,\mathrm{g\,m^{-2}}$ and considerable geometric thickness ($H > 1500\,\mathrm{m}$), HAMP retrieved LWP becomes more representative as the retrieval represents the entire cloud and not only CT properties observed by SMART. Common satellite-

10   based microwave radiometer retrievals of LWP above $180\,\mathrm{g\,m^{-2}}$ are error-prone because of their large footprint. With the smaller footprint of HAMP these uncertainties in LWP are reduced, resulting in a lower uncertainty in retrieved N_{B} and N_{C}. The retrievals of $r_{\mathrm{eff,B}}$ from combined measurements of SMART and HAMP are slightly more prone to the uncertainty of the LWP_{B} measurements and lead to uncertainties of $r_{\mathrm{eff,B}}$ of up to $\pm 1.5\,\mu\mathrm{m}$, being sightly higher than r_{eff} estimated for method A. However, the uncertainty of N with respect to r_{eff} is lower as the sensitivity of N_{B} with respect to $r_{\mathrm{eff,B}}$ is lower

15   in Eq. (12) compared to Eq. (10). The sensitivity study leads to the conclusion, that an appropriate retrieval of r_{eff} is the most important factor for the calculation of N.

For the exemplary ideal adiabatic case study discussed in above, the total uncertainties of the three methods are for $\Delta\,N_{\mathrm{A}} = \pm 7.1\,\mathrm{cm^{-3}}$, $\Delta\,N_{\mathrm{B}} = \pm 14.1\,\mathrm{cm^{-3}}$, and $\Delta\,N_{\mathrm{C}} = \pm 15.1\,\mathrm{cm^{-3}}$. For sub-adiabatic clouds, the uncertainties of method A and B increase due to the assumption of adiabaticity. The additional error in N results from the increased variability in f_{ad}.

20   # 6   Results

The retrieval of N is applied to two measurement cases observed during NARVAL-II. Figure 2 shows the flight track of Research Flight 06 (RF 06) from 19 August 2016 and the flight section (19:24 to 19:39 UTC) of the track for which the remote sensing measurements are analyzed. The satellite image represents the cloud situation at 19:30 UTC. The presence of intense sun-glint is visible, which enhances the reflected radiance $I_{\lambda}^{\uparrow}$ and influences the cloud detection (low contrast) and the retrieval

25   of τ and $r_{\mathrm{eff,A}}$. The analyzed time period is divided into two parts, cloud case #1 and cloud case #2. The north eastern part of the flight track (19:29-19:32 UTC) was dominated by aggregated trade wind cumuli, whereby in the south-western part (19:32-19:36 UTC) shallow cumuli were present. The general weather situation was characterized by moderate convection with low cloud top altitudes. Locally more dense cloud fields formed, at about $10°\,\mathrm{N}$ and $16°\,\mathrm{N}$ at $55°\,\mathrm{W}$.

Time series of measured and retrieved parameters of both cloud cases are shown in Fig. 3 and Fig. 4. The three methods to

30   calculate N assume, that there is no precipitation present. Because measured Z is most sensitive to large cloud droplets, it can not be guaranteed that drizzle is excluded completely. Estimation of the drizzle rate on basis of H and N as proposed by Pawlowska and Brenguier (2003) and vanZanten et al. (2005) is not possible as retrieved N is biased by the process of drizzle formation and, therefore, not applicable with the presented instrument setup of HALO. Flight sections which are flagged for
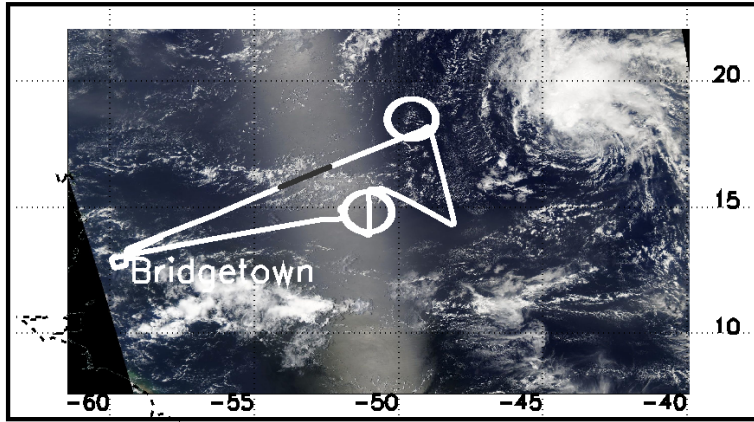
Figure 2. Flight track of HALO (white) from RF 06 (19 August 2016) plotted on a MODIS Terra satellite image from 19:30 UTC. The section for which the remote sensing measurements are analyzed (19:24 UTC to 19:39 UTC) crosses a region with aggregated trade wind cumulus and is plotted in gray.

precipitation are highlighted by the gray boxes. At the top of Fig. 3 and 4 the cloud mask (blue) and the homogeneity cloud flag HCF (yellow) are indicated. Images of RGB composites by specMACS are given in the lower part of the plots to illustrate the visual cloud characteristics. Data gaps are due to cloud free pixel.

6.1 Cloud Case #1

Case #1 represents a stratiform single layer cloud without any convective areas which is an ideal test case for the N retrieval. The cloud optical thickness τ shown in Fig. 3a is generally low and ranges between 0 and 2 at the beginning of the section, while τ increases to up to 6 with time. The uncertainty of τ is estimated to be ± 0.1. The effective radius $r_{\rm eff,A}$ (panel b, black line) ranges between 9.6 μm and 26.3 μm with an uncertainty of $\pm 1.0\,\mu$m, while $r_{\rm eff,B}$ is between 8.3 μm and 30 μm retrieved with a slightly higher uncertainty of $\pm 1.5\,\mu$m. For the first cloud part, the SMART liquid water path $LWP_{\rm A}$ (panel c) is calculated with Eq. (4) using retrieved τ and $r_{\rm eff,A}$. For the first part of the cloud $LWP_{\rm A}$ is slightly lower than the $LWP_{\rm B}$ measured by the microwave profiler, while with increasing τ the agreement between both LWP improves. Vertical profiles of LWC shown in Fig. 3g are below the detection threshold except for four cloud patches. This indicates, that no precipitation was detected, whereby slight drizzle can not be excluded. Cloud base height is estimated from dropsondes to be around 1500 m, while $h_{\rm CT}$ is determined by WALES. The resulting cloud geometric thickness H (Fig. 3d) varies between 100 m and 420 m. Cloud adiabaticity $f_{\rm calc}$ (Fig. 3e) is mostly below 0.5 indicating a considerable sub-adiabatic cloud. Calculated $N_{\rm A}$ and $N_{\rm B}$ are

shown in Fig. 3f and range between $5\,\mathrm{cm}^{-3}$ and $40\,\mathrm{cm}^{-3}$ which results from the low low τ, LWP_B, large $r_\mathrm{eff,A}$, and $r_\mathrm{eff,B}$. The cloud droplet number concentration N_A shows a peak around 19:34:30 UTC and N_A at 19:35:00 UTC. Cloud droplet number concentration N_C derived by method C is lower than N_A and N_B and does show a reduced variability compared to N_A and N_B. However, the uncertainty of all N is about $\pm 15\,\mathrm{cm}^{-1}$. While in the fist part of cloud case #1 the differences in

5   N are large, there is a good agreement between all three methods in the second part where all results are inside the uncertainty range of each method. Mean values of measured and retrieved parameters for cloud case #1 are listed in Table 4.

6.2   Cloud Case #2

The second case represents a more heterogeneous single-layer cloud observed between 19:29 UTC and 19:32 UTC, shown in

10   Fig. 4. This cloud is in a later state of development and shows moderate convection with slight precipitation. In these areas (highlighted in gray), the criteria for cloud homogeneity is not fulfilled. Despite that and the slight precipitation, calculation of N is performed, knowing that the retrieval of N using method A and B are prone to errors under this circumstances. These results are used to evaluate the improvement of retrieved N by method C which accounts for cloud geometry and sub-adiabicity. By comparing convective and non-convective areas of this cloud case #2, the limitations and advantages of the three methods

15   are investigated. Mean values of the measured and retrieved parameters from the three different methods separated for non-precipitation and precipitation are summarized in Table 4.

For the non-precipitating and homogeneous part of cloud case #2, τ does not exceed a value of 30 and $r_\mathrm{eff,A}$ and $r_\mathrm{eff,B}$ range between $18\,\mu\mathrm{m}$ and $40\,\mu\mathrm{m}$ (Fig. 4a, b). The uncertainty of all measured and retrieved parameters, is in a similar range as calculated for cloud case #1. Retrieved LWP from SMART and HAMP (Fig. 4c) agrees within the uncertainty range of

20   HAMP for most parts of the homogeneous cloud sections. Larger differences appear around 19:29:30 UTC where LWP_A is larger than LWP_B. For method C, cloud geometrical thickness H is calculated from a combination of HAMP and WALES. Radar reflectivity Z is above the precipitation detection threshold of $-20\,\mathrm{dBZ}$ and allows to determine vertical profiles of the LWC and h_CB with an average value of $h_\mathrm{CB} \approx 900\,\mathrm{m}$ where no precipitation is present. Cloud top height h_CT from WALES ranges between $200\,\mathrm{m}$ and $1000\,\mathrm{m}$ for the non-precipitating regions. This results in a highly variable f_calc, which

25   varies between strongly varies between 0.05 and 1.0.

Cloud droplet number concentration from method A and B calculated for cloud case #2 are generally low (see also Table 4) mostly ranging between $20\,\mathrm{cm}^{-3}$ and $40\,\mathrm{cm}^{-3}$. Together with large $r_\mathrm{eff,A}$ and $r_\mathrm{eff,B}$ these values indicate typical pristine maritime clouds. An exception is observed around 19:29:30 UTC where N peaks up to $120\,\mathrm{cm}^{-3}$ for all three methods mostly resulting from a decrease of $r_\mathrm{eff,A}$ and an increase of τ. The decrease of r_eff might result from 3D-radaitive effects at the cloud

30   edge overestimating the cloud particle size and can have biased the retrieval of N.

In the areas marked with precipitation, retrieved τ, LWP_A, and LWP_B are higher compared to the precipitation free regions while $r_\mathrm{eff,A}$ and $r_\mathrm{eff,B}$ are in the same range as for the non-precipitating areas. In contrast to the homogeneous parts of the cloud, the convective regions show stronger horizontal heterogeneity in all parameters. The optical thickness reaches up to 40 and $r_\mathrm{reff,A}$ ranges from $20\,\mu\mathrm{m}$ to $38\,\mu\mathrm{m}$. In these areas the LWP_B from HAMP exceeds $270\,\mathrm{g\,m}^{-2}$ and shows a maximum
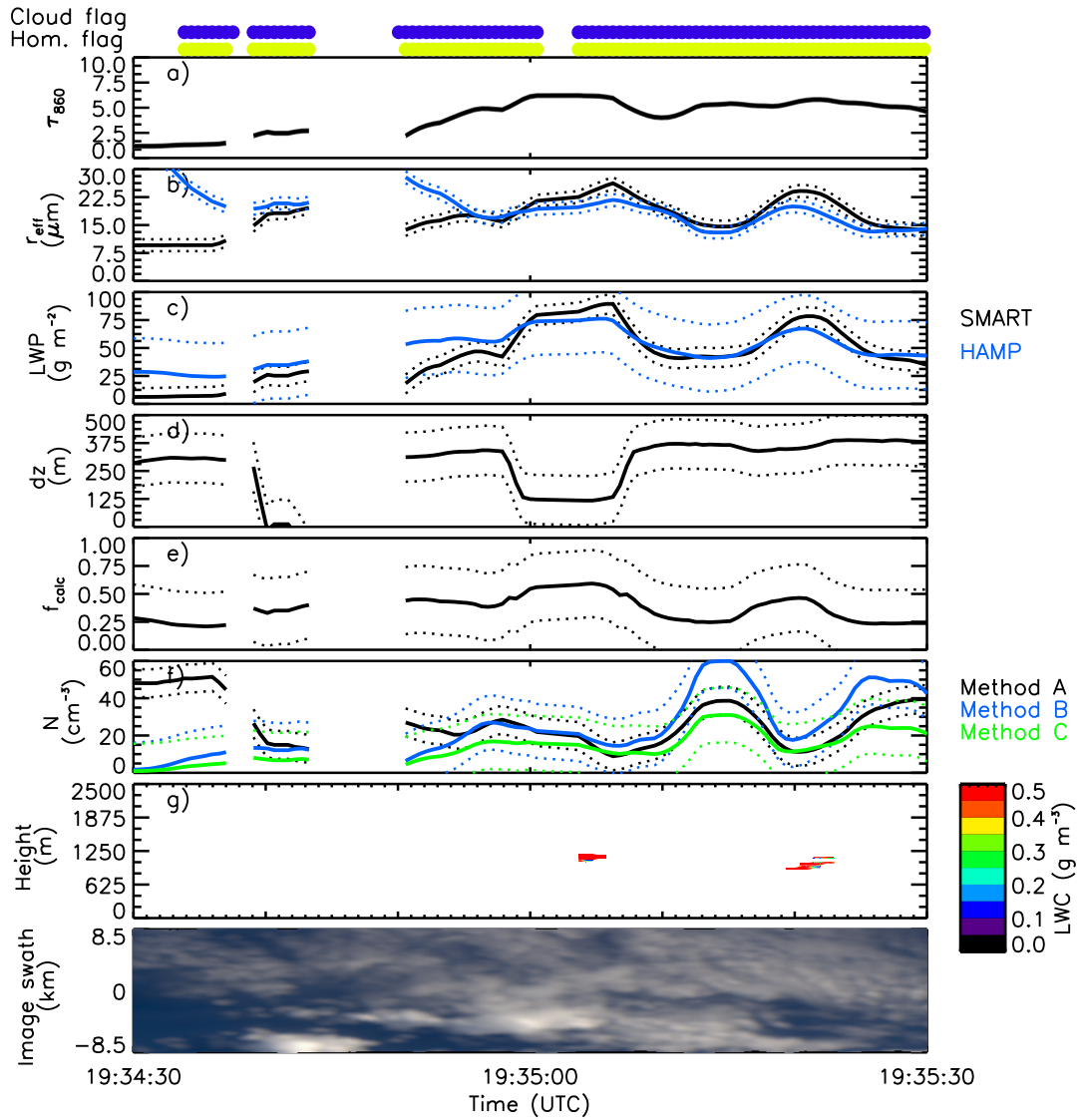
Figure 3. Time series of measured and retrieved cloud properties of cloud case #1 from 19:34:30 to 19:35:30 UTC of RF06. Cloud droplet number concentration N is shown for all three methods A, B, and C. Uncertainty ranges of the individual parameters are indicated by dotted lines. At the top, the cloud mask (blue) and the homogeniety cloud flag (HCF) (yellow) derived by SMART are indicated.

Table 4. Mean values of cloud properties of cloud cases #1 and #2.

parameter	Cloud case #1	Cloud case #2 (np)	Cloud case #2 (p)
τ	4.3	3.5	11.3
$r_{\mathrm{eff,A}}$ [μm]	17.1	30.4	24.9
$r_{\mathrm{eff,B}}$ [μm]	19.2	29.1	23.4
LWP_{A} [$\mathrm{g\,m^{-2}}$]	45	135	226
LWP_{B} [$\mathrm{g\,m^{-2}}$]	50	120	210
H [m]	315	959	1315
N_A [$\mathrm{cm^{-3}}$]	27	17	47
N_B [$\mathrm{cm^{-3}}$]	26	25	53
N_C [$\mathrm{cm^{-3}}$]	19	13	40

value up to $500\,\mathrm{g\,m^{-2}}$. Liquid water path from SMART is in the same range of LWP_{B} except for the first precipitation section (19:30:30 UTC) where LWP_{B} is lower than LWP_{A}. For the precipitating regions the cloud base height h_{CB} is assumed to be at the same level as determined for the non-precipitating regions as precipitation makes the cloud base invisible for the radar. The cloud geometric thickness H is slightly higher for the connective regions and ranges between 800 m and 1300 m. The

5 calculated adiabaticity f_{calc} is lower than 0.5 for the majority of the measurement and shows that most parts of the cloud are sub-adiabatic. For the precipitation regions calculated N are between $10\,\mathrm{cm^{-3}}$ and $90\,\mathrm{cm^{-3}}$ with the highest concentrations for method B, followed by method A and the lowest N for method C. In the areas with precipitation, N shows a systematic higher variability which is observed by all three methods and likely caused by the variability of r_{eff} retrieved from SMART. One reason for this variability is the relation of r_{vol} to r_{reff} which is assumed to be (i) constant in the retrieval of r_{A} and r_{B}

10 and (ii) significantly influenced by formation of precipitation. Therefore, calculated N by all three methods are highly prone to errors for precipitating clouds. The variability of N might also be caused by intense turbulent mixing processes within the cloud. Concluding from that, it is suggested to filter areas with stronger convection, precipitation, and heterogeneous scenes and analyze the retrieved N with special care.

6.3   Statistical Analysis of Liquid Water Path, Droplet Effective Radius, and Number Concentration

15 Statistics of retrieved cloud properties are analyzed for measurements between 19:24:00 UTC and 19:39:00 UTC only, where the HCF indicates homogeneous clouds and uncertainties of the retrieved cloud parameters are low. An extension of the analysis to other flights is not possible yet, because the reliable application of the retrieval of N requires careful data selection and good quality data of all individual instruments. However, in total 700 individual measurements are included which represents a cloud field of 77 km length. The clouds were separated into precipitating (p) and non-precipitating (np) pixel. Mean values

20 of the parameters for each measurement are summarized in Tab. 4.

Figure 5 compares measurements of LWP_{A} and LWP_{B}. The data is separated for different $r_{\mathrm{eff,A}}$ split into bins of 5 μm size.
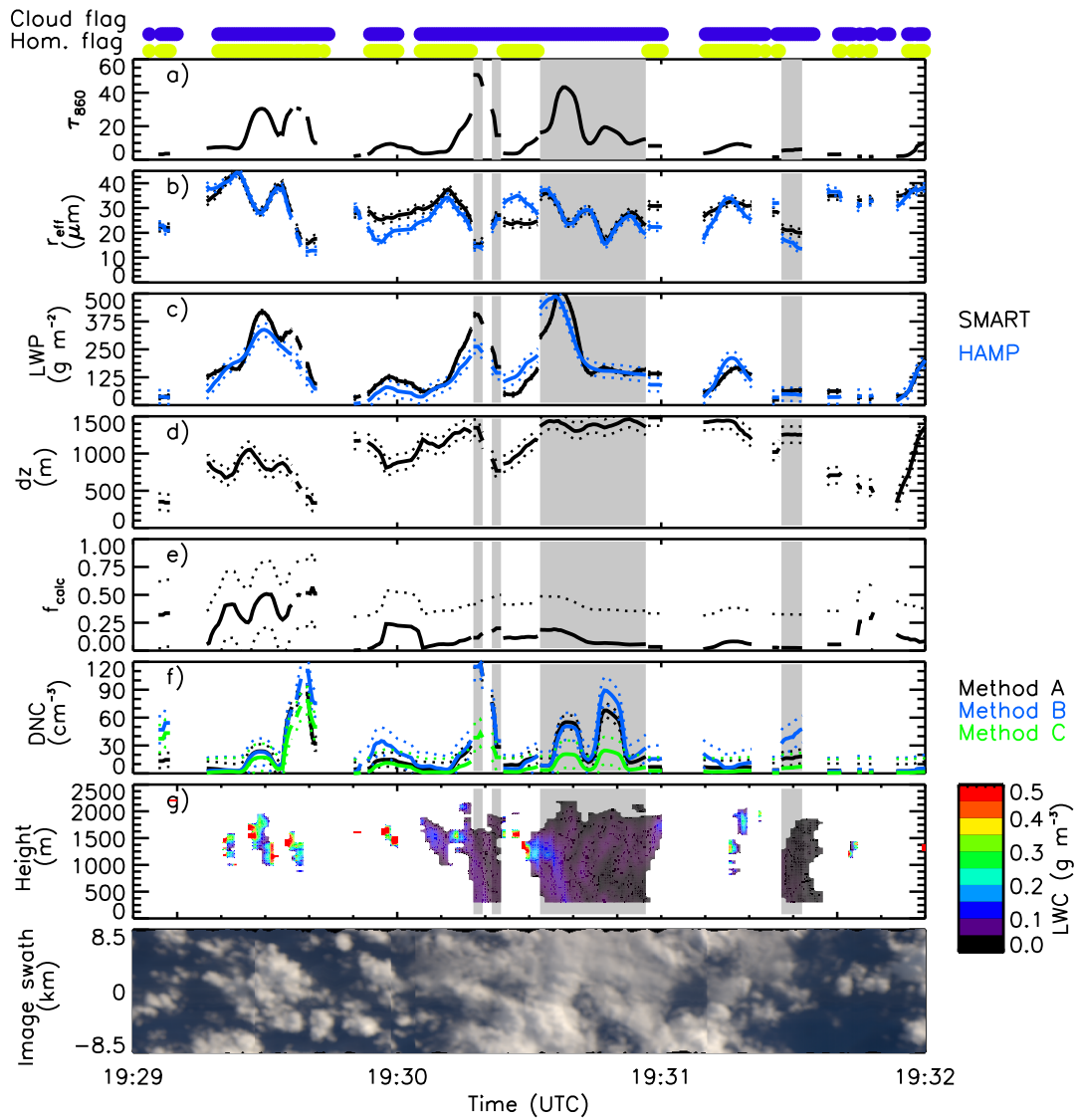
Figure 4. Time series of measured and retrieved cloud properties of cloud case #1 from 19:29 to 19:32 UTC of RF06. Cloud droplet number concentration N is shown for all three methods A, B, and C. Uncertainty ranges of the individual parameters are indicated by dotted lines. At the top, the cloud mask (blue) and the homogeneity cloud flag (HCF) (yellow) derived by SMART are indicated.
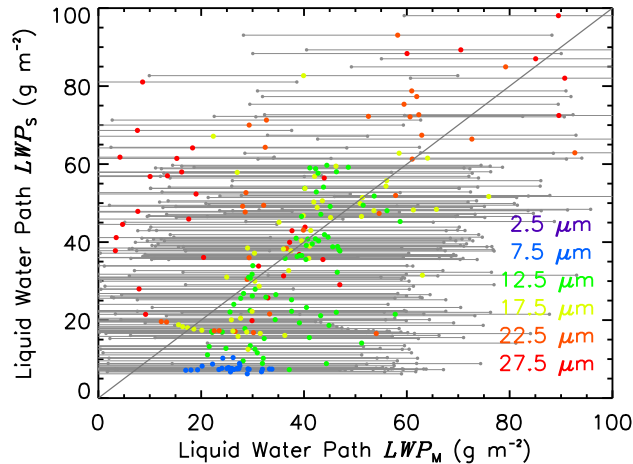
Figure 5. Comparison of liquid water path LWP_B from HAMP microwave radiometer and LWP_A calculated from τ and $r_{\mathrm{eff,A}}$ retrieved by SMART. The color code indicates different ranges of $r_{\mathrm{eff,A}}$. HAMP uncertainties of LWP ($\pm 30\,\mathrm{g\,m^{-2}}$) are indicated by gray errors bars.

For the selected time period, LWP_A agrees with LWP_B within the uncertainty range of HAMP of $\pm 30\,\mathrm{g\,m^{-2}}$ indicated by the gray error bars. The differences of LWP_A and LWP_B show a larger variability for clouds with large $r_{\mathrm{eff,A}}$ than for clouds with small $r_{\mathrm{eff,A}}$. For larger cloud droplets, the retrieval uncertainty of τ and $r_{\mathrm{eff,A}}$ increases and, therefore, also LWP_A derived from SMART. Additionally, SMART has a higher sensitivity to droplets at cloud top and the FOV of HAMP is slightly

5   larger compared to SMART what can explain some of the observed variability. Slightly different viewing directions have to be considered too. While for SMART the LWP_A is calculated assuming an adiabatic profile with the retrieved $r_{\mathrm{eff,A}}$ representing cloud top, HAMP obtains an integrated measure of LWP where all cloud layers are more homogeneously weighted and no assumption on the cloud profiles is required. Therefore, a difference between LWP_A and LWP_B indicates that the observed clouds are non-adiabatic. For $LWP_A > LWP_B$ less liquid water is at CB than predicted by adiabatic theory and clouds are

10 sub-adiabatic. For $LWP_A < LWP_B$ liquid water at CT is reduced, likely by precipitation as supported by the preferred r_{eff} in these LWP regime (Fig. 5).

Figures 6a and b show the normalized probability density function (PDF) of LWP retrieved by HAMP and SMART separated for precipitating and non-precipitating clouds. For the non-precipitating clouds, the distributions of LWP retrieved by SMART and HAMP are dominated by clouds below $100\,\mathrm{g\,m^{-2}}$. Higher LWP are obtained for regions with precipitation, where the distribution is shifted towards larger values of LWP. The PDF of LWP_A and LWP_B show a dominant mode at

15 around $150\,\mathrm{g\,m^{-2}}$. A second smaller mode is present for LWP_A at $80\,\mathrm{g\,m^{-2}}$ and LWP_B at $50\,\mathrm{g\,m^{-2}}$ for both instruments. The agreement of the LWP retrievals, utilizing reflected solar radiation from CT (method A) and passive microwave measurements (method B), indicate that the cloud microphysical properties are sufficiently determined by the SMART retrieval,

Table 5. Measured and retrieved properties of the entire period of both cloud cases, separated for precipitating (p) and non-precipitating (np) clouds.

	$\overline{\tau}$	$\tau_{\mathrm{med,S}}$	$\overline{r}_{\mathrm{eff,A}}$	$r_{\mathrm{eff,med,A}}$	$\overline{h}_{\mathrm{ct,L}}$	$\overline{N}_{\mathrm{A}}$	$\overline{N}_{\mathrm{A,med}}$	$\overline{N}_{\mathrm{B}}$	$\overline{N}_{\mathrm{B,med}}$	$\overline{LWP}_{\mathrm{A}}$	$\overline{LWP}_{\mathrm{B}}$
np	3.5	2.2	23.2 μm	21.1 μm	1798 m	17 cm^{-3}	14 cm^{-3}	25 cm^{-3}	12 cm^{-3}	72 g m^{-3}	82 g m^{-3}
p	11.3	7.0	25.1 μm	24.5 μm	1988 m	47 cm^{-3}	17 cm^{-3}	53 cm^{-3}	25 cm^{-3}	170 g m^{-3}	203 g m^{-3}
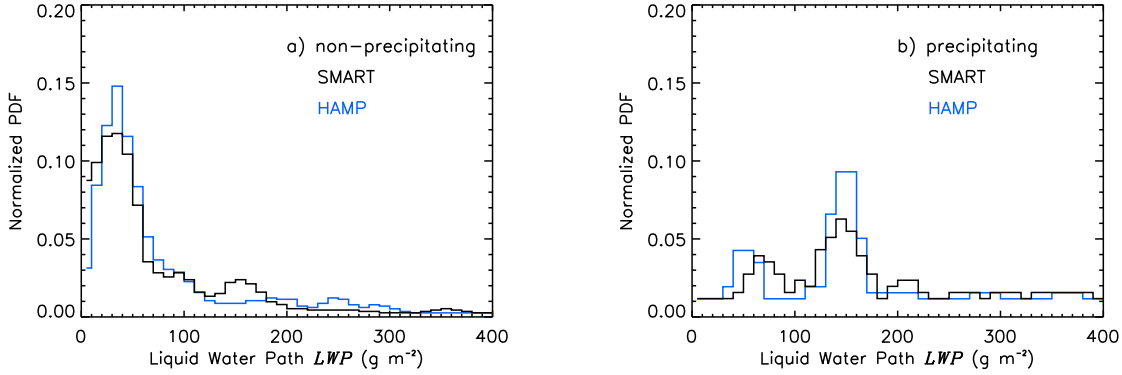
Figure 6. Normalized probability density function (PDF) of measured and calculated liquid water path LWP from HAMP (blue) and SMART (black). Distributions are filtered for non-precipitating a) and precipitating b) clouds.

despite the assumption of an adiabatic cloud profile in method A.

In Fig. 7 the normalized PDF of $r_{\mathrm{eff,A}}$ retrieved from SMART only (method A) and $r_{\mathrm{eff,B}}$ retrieved synergistically from SMART and HAMP (method B) separated for precipitating and non-precipitating clouds are presented. The mean value for non-precipitating clouds is around $\overline{r}_{\mathrm{eff,A,np}} = 23.2\ \mu$m and the median is at $r_{\mathrm{eff,A,np,med}} = 21.1\ \mu$m. This droplet size range agrees with in-situ measurements of pristine trade wind cumulus by Siebert et al. (2013) and remote sensing measurements by Werner et al. (2014) in the same geographic region. The distribution shows a bi-modal structure with a first mode around 15 μm and a second mode around 32 μm. The PDF of $r_{\mathrm{eff,A}}$ for precipitation situations shows a similar structure being shifted towards larger $r_{\mathrm{eff,A}}$ with values of $\overline{r}_{\mathrm{eff,A,p}} = 25.1\ \mu$m and $r_{\mathrm{eff,A,p,med}} = 24.5\ \mu$m. The first mode is at 21 μm and the second mode is at 36 μm. The PDF's of $r_{\mathrm{eff,B}}$ for the np clouds are shifted to larger values by approximately 3 μm additionally showing a third mode around 38 μm. In contrast, the PDF for the p clouds is shifted to lower values by up to 8 μm and showing only the bi-modal structure with peaks around 15 μm and 33 μm.

Figures 8a and b show normal normalized PDF of the calculated N for non-precipitating (a) and precipitating regions (b) of the selected flight-leg from all three methods A, B, and C. For non-precipitating clouds (panel 8a) the distribution of N_{A} peaks at $N_{\mathrm{A}} \approx 30$ cm^{-3} with a steep decrease towards a concentration of ≈ 100 cm^{-3}. The first local maximum of the N_{B} distribution
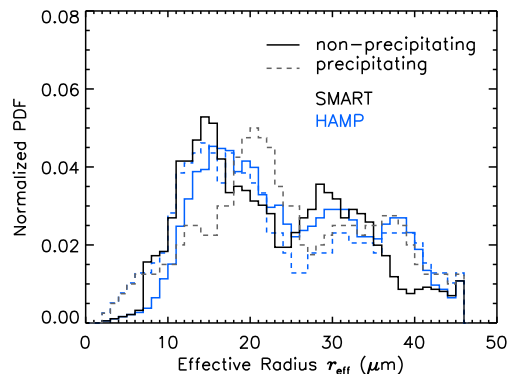
Figure 7. Normalized probability density function (PDF) of the effective radius $r_{\mathrm{eff,A}}$ retrieved by using the ratio of 1645 nm to 1050 nm in black and $r_{\mathrm{eff,B}}$ from the combined spectrometer-microwave retrieval in blue. Distributions are filtered for non-precipitating (solid line) and precipitating (dashed line) clouds.

is at $N_{\mathrm{B}} \approx 30\,\mathrm{cm}^{-3}$ slowly decreasing for larger N. Only a slight difference between N_{A} and N_{B} is present for higher N_{A}. This can be explained by the slightly higher values of SMART LWP_{A} compared to HAMP LWP_{B}. The PDFs of N_{A} and N_{B} show reasonable results for pristine, maritime clouds with relative large $r_{\mathrm{eff,A}}$ and according low N from method A and B. Cloud droplet number concentration from method C are significantly lower as a result of the considered adiabaticity of the

5 individual clouds.

Measurements affected by precipitation compared to Fig. 8a show almost the same distribution with a shift to larger N for all three calculation methods, especially for method C. Filtering for precipitating clouds the statistic might be biased by only considering further developed clouds in which precipitation formation changes and broadens the droplet size distribution. This leads to differences in the means of r_{vol} and r_{eff}, influencing the k-parameter which is assumed to be 0.8 in the N calculation.

10 Retrieving k by passive remote sensing is not possible yet (Wood, 2006).

Figure 9 shows the cloud top reflectivity $\mathcal{R}_{532}$ measured by SMART at 532 nm as a function of N_{B} retrieved from combined SMART and HAMP measurements. Only measurements of the flight leg where no precipitation was observed are presented. The data is binned for two different LWP. Figure 9a shows clouds with LWP between $0-50\,\mathrm{g\,m}^{-2}$ and Fig. 9b shows clouds in the range between $50-100\,\mathrm{g\,m}^{-2}$. Colors represent $r_{\mathrm{eff,B}}$ binned from 5 to 30 μm in 5 μm steps (label in Fig. 9

15 refers to the mean bin value). Using $\mathcal{R}_{532}$ as a measure for the reflectivity of the cloud, the sensitivity of $\mathcal{R}_{532}$ on changes of N is comparable to the model based sensitivity study in Section 2. Therefore, in Fig. 9 radiative transfer simulations of theoretical $\mathcal{R}_{532,\mathrm{sim}}$ for clouds of the same LWP are added by the red line. For the thin clouds in Fig. 9a the measured $\mathcal{R}_{532}$ shows a clear increase for higher N_{B} over the entire measurement range. This correlation is less pronounced for the thicker clouds in Fig. 9b due to a reduced range of $\mathcal{R}_{532}$ and N, where the observations may not cover the entire natural variability. However,

20 for both cloud sub-samples, the measurements follow the theoretical line given by the simulations only that the measured
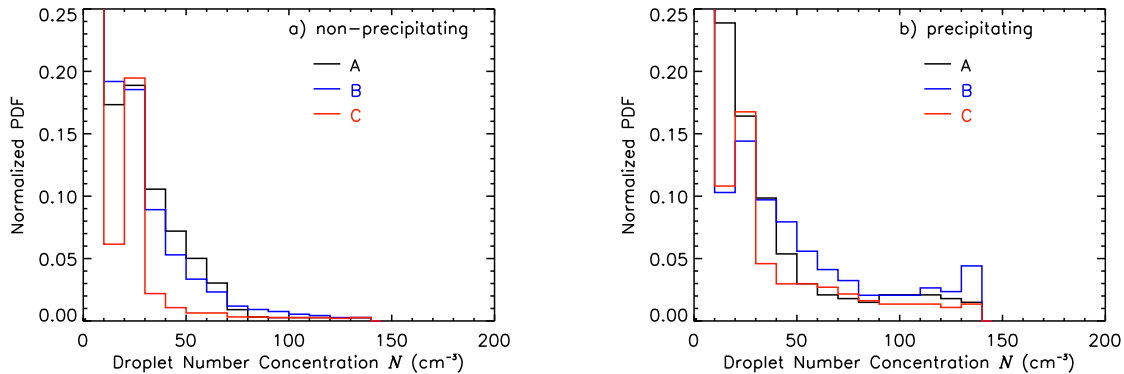
Figure 8. Normalized probability density function of the cloud droplet number concentration N for the selected flight path using method A, B, and C. Distributions are filtered for non-precipitating a) and precipitating b) clouds.
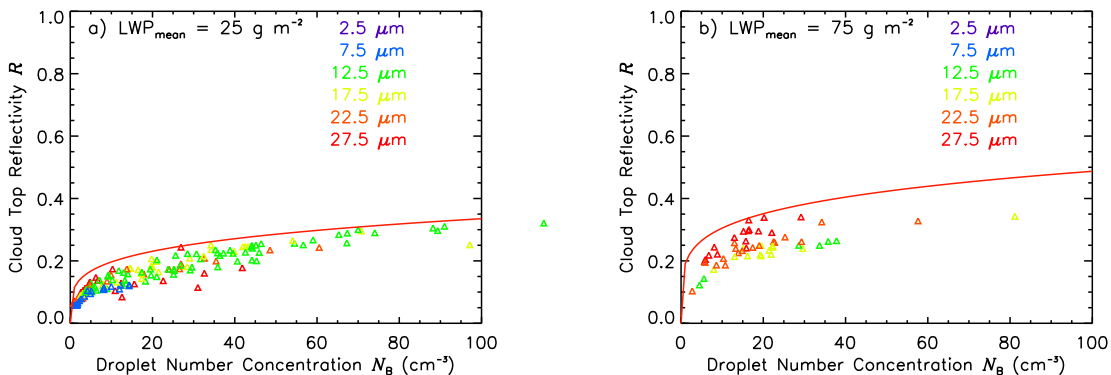
Figure 9. Cloud top reflectivity $\mathcal{R}_{532}$ as a function of cloud droplet number concentration N_{B} for homogeneous, non-precipitating clouds of different liquid water path LWP_{B} (panel a: $0 - 50\,\mathrm{g\,m^{-2}}$, panel b: $50 - 100\,\mathrm{g\,m^{-2}}$). The droplet effective radius r_{eff} of each measurement is indicated by the color code. The red line represents simulated reflectivity $\mathcal{R}_{532}$ from radiative transfer calculations for clouds with same LWP.

$\mathcal{R}_{532}$ are too low or retrieved N to high. Both might be attributed to measurement biases either the radiometric calibration of SMART or the retrieved LWP_{B} and $r_{\mathrm{eff,B}}$ which feed the calculation of N_{B}. Additionally, the homogeneous assumption of cloud properties applied in the RTS can lead to an overestimation of $\mathcal{R}_{532,\mathrm{sim}}$ compared to the measurements. The subdivision of data for different $r_{\mathrm{eff,B}}$ shows that clouds in an early developing state with low LWP_{B} (Fig. 9a) are dominated by smaller cloud droplets up to $r_{\mathrm{eff,B}} = 17.5\,\mu\mathrm{m}$ whereby clouds in a later development state with higher LWP_{B} (Fig. 9b) are dominated

by cloud droplets larger than $r_{\mathrm{eff,B}} = 17.5\,\mu\mathrm{m}$.

7 Conclusions

Trade wind cumuli are an ubiquitous cloud type in the tropics influencing the Earth radiative energy budget significantly. In spite of their importance, they are not appropriately represented in numerical weather prediction (NWP) and global climate models (GCMs), causing considerable uncertainties in the radiation schemes of the models. Platnick and Twomey (1994) showed that the cloud top albedo α of clouds with low cloud droplet number concentration N and low liquid water path LWP, such as trade wind cumuli, respond sensitively to changes of N. In order to obtain improved parameterizations and global distributions of N, several methods, including active and passive remote sensing from ground and satellite are developed, but no operational products are available yet. Only a limited number of field campaigns with in-situ measurements of selected cloud cases exist. As a result, the natural variability of trade wind cumulus is poorly covered by appropriate measurements.

Sensitivity simulations in this paper show that shallow trade wind cumuli with LWP below $200\,\mathrm{g\,m^{-2}}$ and N below $100\,\mathrm{cm^{-3}}$ are very sensitive to changes in N. In case of a LWP of $75\,\mathrm{g\,m^{-2}}$, an increase of N from $50\,\mathrm{cm^{-3}}$ to $100\,\mathrm{cm^{-3}}$, leads to an increase of α by 0.1. Therefore, the influence of trade wind cumuli on the Earth radiation energy budget is variable and significantly depends on the interaction between α, N, cloud optical thickness τ, cloud droplet effective radius r_{eff}, and different thermodynamic conditions (e.g. varying LWP), which has to be investigated systematically.

Applying the common satellite retrieval techniques of N to measurements conducted with a high flying aircraft, such as the High Altitude and Long Range Research Aircraft (HALO), shows the potential of combined airborne passive and active remote sensing instruments. Using aircraft instead of satellite platforms allows to investigate specific cloud types under selected atmospheric conditions, e.g., cloud top temperature T_{CT}, cloud top pressure p_{CT}, and LWP.

This was done during the second campaign of the Next Generation Remote Sensing for Validation Studies (NARVAL-II), where HALO was equipped with a set of passive and active remote sensing instruments. The Spectral Modular Airborne Radiation measurement sysTem (SMART) measured upward and downward spectral irradiance $F_\lambda^{\uparrow\downarrow}$ and upward radiance $I_\lambda^\uparrow$, which enables to calculate α and retrieve τ and $r_{\mathrm{eff,A}}$ at cloud top. The HALO Microwave Package (HAMP) enables to perform retrievals of LWP and radar reflectivity Z used to separate for bins of LWP and to discriminate between non-precipitating and precipitating cloud sections. Combining measured values of $I_\lambda^\uparrow$ by SMART and LWP by HAMP, alternative values of r_{eff} are retrieved, which are less influenced by 3D cloud radiative effects. Cloud top height h_{CT} is determined by the Water Vapour Lidar Experiment in Space (WALES) while the cloud base height h_{CB} is estimated from dropsondes or radar data.

The heterogeneity of shallow trade wind cumulus fields during NARVAL-II has to be considered in the analysis. This is especially important in the retrieval of τ, r_{eff}, and N at the average flight speed of HALO ($v_{\mathrm{ac}} \approx 220\,\mathrm{m\,s^{-1}}$) and different instrument field-of-views (FOV), being in the size range of individual clouds. The heterogeneity is indicated by the high occurrence ($63\,\%$) of clouds with a horizontal size smaller than 300 m. In this context, a careful cloud masking and filtering for homogeneous cloud regions is crucial. Using cloud flagging and masking, the calculation of N can be applied to approximately $55\,\%$ of all observed clouds.

Three different methods to retrieve N based on Eq. (10) are presented and the application is shown for synthetic measurements of six different clouds with N_{cld} of $50\,\mathrm{cm^{-3}}$, $100\,\mathrm{cm^{-3}}$, and $200\,\mathrm{cm^{-3}}$ each following an adiabatic and sub-adiabatic cloud

Table 6. List of symbols, longnames and related units.

Symbol	Longname	Unit
α	Cloud top albedo	-
D	Cloud droplet diameter	m
H	Cloud geometric thickness	m
f_{ad}	Degree of adiabaticity	-
$F_\lambda^\uparrow$	Spectral upward radiance	$\mathrm{W\,m^{-2}\,nm^{-1}}$
$F_\lambda^\downarrow$	Spectral downward radiance	$\mathrm{W\,m^{-2}\,nm^{-1}}$
Γ_{ad}	Adiabatic rate of liquid water content	$\mathrm{kg\,m^{-3}\,m^{-1}}$
Γ_{calc}	Calculated rate of liquid water content	$\mathrm{kg\,m^{-3}\,m^{-1}}$
h_{CB}	Cloud base height	m
h_{LCL}	Lifting condensation level	m
h_{CT}	Cloud top height	m
$I_{\mathrm{cr}}^\uparrow$	Spectral upward irradiance threshold	$\mathrm{W\,m^{-2}\,nm^{-1}\,sr^{-1}}$
$I_\lambda^\uparrow$	Spectral upward irradiance	$\mathrm{W\,m^{-2}\,nm^{-1}\,sr^{-1}}$
$I_{\lambda,\mathrm{syn}}^\uparrow$	Spectral upward irradiance (simulated)	$\mathrm{W\,m^{-2}\,nm^{-1}\,sr^{-1}}$
k	k-parameter	-
l_{cld}	Cloud length	m
LWC	Liquid water content	$\mathrm{kg\,m^{-3}}$
LWP	Liquid water path	$\mathrm{kg\,m^{-2}}$
LWP_{A}	Liquid water path from SMART	$\mathrm{kg\,m^{-2}}$
LWP_{B}	Liquid water path from HAMP	$\mathrm{kg\,m^{-2}}$
N	Cloud droplet number concentration	$\mathrm{cm^{-3}}$
N_{cld}	Cloud droplet number concentration of simulated clouds	$\mathrm{cm^{-3}}$
p_{CT}	Cloud top pressure	Pa
Q	Extinction coefficient	-
$\mathcal{R}$	Cloud top reflectivity	-
p_{CT}	Cloud top pressure	Pa
ρ_{w}	Density of liquid water	$\mathrm{kg\,m^{-3}}$
r_{eff}	Effective radius	$\mu\mathrm{m}$
$r_{\mathrm{eff,A}}$	Effective radius from SMART	$\mu\mathrm{m}$
$r_{\mathrm{eff,B}}$	Effective radius from SMART & HAMP	$\mu\mathrm{m}$
r_{vol}	Volumetric radius	$\mu\mathrm{m}$

Symbol	Longname	Unit
τ	Cloud optical thickness from SMART	-
τ_{lib}	Cloud optical thickness from libRadtran	-
T	Temperature	$^\circ$C
T_{d}	Dew-point temperature	$^\circ$C
T_{CT}	Cloud top temperature	$^\circ$C
t_{int}	Integration time of spectrometer	s
v_{ac}	Aircraft velocity	$\mathrm{m\,s^{-1}}$
ϑ	Solar zenith angle	$^\circ$
Z	Radar reflectivity	dBz
ζ	Cloud top albedo sensitivity	$\mathrm{cm^3}$

profile. From the synthetic measurements it can be concluded that the calculation of N on basis of τ and $r_{\mathrm{eff,A}}$ from SMART method A is suggested for optically thin clouds with ($LWP < 100\,\mathrm{g\,m^{-2}}$) while for optically thicker clouds method B is preferred, where τ is replaced by LWP retrieved by HAMP. For homogeneous clouds when the cloud boundaries can be determined precisely from the active radar, lidar, and dropsonde measurements, the resulting calculated adiabaticity factor

5   Γ_{calc} can be determined and used as a correction factor in the calculation of N as the optimal case (method C). The synthetic measurements further showed that the differences between modeled N_{cld} and retrieved $N_{\mathrm{C,lib}}$ or $N_{\mathrm{C,R}}$ with method C, are significantly reduced comparing to method A or B, for all three cloud cases. This indicates that a correction with Γ_{calc} is vital and necessary for the calculation of N of shallow trade wind cumuli using remote sensing techniques. Otherwise systematic overestimation of retrieved N is present and not feasible.

10   Subsequently, the three methods are applied to a homogeneous and a heterogeneous cloud section. Both cloud cases are statistically analyzed. Determination of the cloud geometric thickness H was relatively uncertain in both cases and method C was excluded from the statistical analysis. Probability density functions of LWP, r_{eff}, and N of the two cloud scenes are presented. Correlations of cloud top reflectivity $\mathcal{R}_{532}$ at 532 nm to N_{B} for two binned LWP_{B} are shown. These are used to validate modeled $\mathcal{R}_{532}$, to describe the sensitivity of $\mathcal{R}_{532}$ with respect to N, and allow to parameterize the Twomey effect. Comparison

15   of simulated and measured $\mathcal{R}_{532}$ showed systematic lower values of observed $\mathcal{R}_{532}$. Further testing of the proposed method to longer flight sections is necessary, to cover the natural variability of trade wind cumuli and thermodynamical conditions. Despite remaining uncertainties and assumptions, the application of Γ_{calc}, the separation for different LWP, and the smaller FOV of all instruments, allow to investigate the cloud-radiation interactions better compared to large-scale averaging satellite measurements.

Acknowledgements. This research was funded by the German Research Foundation (DFG, HALO-SPP 1294). The authors acknowledge the support by the Deutsche Forschungsgemeinschaft (DFG) through grants CR 111/10-1, PF 384/7-1/2, PF 384/16-1, and WE 1900/35-1), the Max Planck Society, and the German Aerospace Center (DLR). Special thanks also go to Felix Ament and Heike Konow who have provided the calibrated HAMP radar and microwave data. Additionally, the authors thank the pilots and appreciate the support by the Flugbereitschaft

5   of DLR and *enviscope GmbH* for preparation and testing of SMART.

References

Ackerman, A., Toon, O., Taylor, J., Johnson, D., Hobbs, P., and Ferek, R.: Effects of aerosols on cloud albedo: Evaluation of Twomey's parameterization of cloud suszeptibility using measurements of ship tracks, J. Atmos. Sci., 57, 2684–2695, 2000.

Albrecht, B. A.: Aerosols, Cloud Microphysics, and fractional Cloudiness, Science, 245, 1227–1230, http://www.sciencemag.org/content/245/4923/1227.abstract, 1989.

Albrecht, B. A.: Fractional cloudiness and cloud-top entrainment instability, J. Atmos. Sci., 48, 1519–1525, doi:10.1175/1520-0469(1991)048<1519:FCACTE>2.0.CO;2, 1991.

Austin, R. T. and Stephens, G. L.: Retrieval of stratus cloud microphysical parameters using millimeter-wave radar and visible optical depth in preparation for CloudSat: 1. Algorithm formulation, J. Geophys. Res. Atmos., 106, 28 233–28 242, doi:10.1029/2000JD000293, 2001.

Baumgardner, D., Brenguier, J.-L., Bucholtz, A., Coe, H., DeMott, P., Garrett, T., Gayet, J.-F., Hermann, M., Heymsfield, A., Korolev, A., Krämer, M., Petzold, A., Strapp, W., Pilewskie, P., Taylor, J., Twohy, C., and Wendisch, M.: Airborne instruments to measure atmospheric aerosol particles, clouds and radiation: A cook's tour of mature and emerging technology, Atmos. Res., 102, 10–29, doi:10.1016/j.atmosres.2011.06.021, 2011.

Bennartz, R. and Rausch, J.: Global and regional estimates of warm cloud droplet number concentration based on 13 years of AQUA-MODIS observations, Atmos. Chem. Phys., 17, 9815–9836, doi:10.5194/acp-17-9815-2017, 2017.

Bierwirth, E., Wendisch, M., Ehrlich, A., Heese, B., Tesche, M., Althausen, D., Schladitz, A., Müller, D., Otto, S., Trautmann, T., Dinter, T., von Hoyningen-Huene, W., and Kahn, R.: Spectral surface albedo over Morocco and its impact on the radiative forcing of Saharan dust, Tellus, 61B, 252–269, 2009.

Boers, R., Jensen, J. B., and Krummel, P. B.: Microphysical and radiative structure of marine stratocumulus clouds over the Southern Ocean: Summer results and seasonal differences, Q. J. R. Meteorol. Soc., 124, 151–168, 1998.

Boers, R., Acarreta, J. R., and Gras, J. L.: Satellite monitoring of the first indirect aerosol effect: Retrieval of the droplet concentration of water clouds, J. Geophys. Res., 111, D22 208, doi:10.1029/2005JD006838, 2006.

Bony, S. and Dufresne, J.-L.: Marine boundary layer clouds at the heart of tropical cloud feedback uncertainties in climate models, Geophys. Res. Lett., 32, doi:10.1029/2005GL023851, 2005.

Bony, S., Stevens, B., Frierson, D. M. W., Jakob, C., Kageyama, M., Pincus, R., Shepherd, T. G., Sherwood, S. C., Siebesma, A. P., Sobel, A. H., Watanabe, M., and Webb, M. J.: Clouds, circulation and climate sensitivity, Nat. Geosci., 8, 261–268, doi:10.1038/ngeo2398, 2015.

Brenguier, J.-L., Pawlowska, H., Schüller, L., Preusker, R., Fischer, J., and Fouquart, Y.: Radiative properties of boundary layer clouds: Droplet effective radius versus number concentration, J. Atmos. Sci., 57, 803–821, 2000.

Brückner, M., Pospichal, B., Macke, A., and Wendisch, M.: A new multispectral cloud retrieval method for ship-based solar transmissivity measurements, J. Geophys. Res. Atmos., 119, 11.338–11.354, doi:10.1002/2014JD021775, 2014.

Cahalan, R., Silberstein, D., and Snider, J.: Liquid water path and plane-parallel albedo bias during ASTEX, J. Atmos. Sci., 52, 3002–3012, 1995.

Chertock, B., Fairall, C. W., and White, A. B.: Surface-based measurements and satellite retrievals of broken cloud properties in the equatorial Pacific, J. Geophys. Res. Atmos., 98, 18 489–18 500, doi:10.1029/93JD01737, 1993.

Eastman, R., Warren, S. G., and Hahn, C. J.: Variations in cloud cover and cloud types over the ocean from surface observations, 1954-2008, J. Climate, 24, 5914–5934, doi:10.1175/2011JCLI3972.1, 2011.

Elsaesser, G. S., O'Dell, C. W., Lebsock, M. D., Bennartz, R., Greenwald, T. J., and Wentz, F. J.: The multisensor advanced climatology of liquid water path (MAC-LWP), J. Climate, 30, 10 193–10 210, doi:10.1175/JCLI-D-16-0902.1, 2017.

Emde, C., Buras-Schnell, R., Kylling, A., Mayer, B., Gasteiger, J., Hamann, U., Kylling, J., Richter, B., Pause, C., Dowling, T., and Bugliaro, L.: The libRadtran software package for radiative transfer calculations (version 2.0.1), Geosci. Model Dev., 9, 1647–1672, doi:10.5194/gmd-9-1647-2016, 2016.

Espy, J. P.: Essays on meteorology. No. IV, J. Franklin Inst., 22, 239 – 246, doi:https://doi.org/10.1016/S0016-0032(36)91215-2, 1836.

Ewald, F., Kölling, T., Baumgartner, A., Zinner, T., and Mayer, B.: Design and characterization of specMACS, a multipurpose hyperspectral cloud and sky imager, Atmos. Meas. Tech., 9, 2015–2042, doi:10.5194/amt-9-2015-2016, 2016.

Frisch, A. S., Martner, B. E., Djalalova, I., and Poellot, M. R.: Comparison of radar/radiometer retrievals of stratus cloud liquid-water content profiles with in situ measurements by aircraft, J. Geophys. Res. Atmos., 105, 15 361–15 364, doi:10.1029/2000JD900128, 2000.

Grosvenor, D. P., Sourdeval, O., and Wood, R.: Parameterizing cloud top effective radii from satellite retrieved values, accounting for vertical photon transport: quantification and correction of the resulting bias in droplet concentration and liquid water path retrievals, Atmos. Meas. Tech., 11, 4273–4289, doi:10.5194/amt-11-4273-2018, 2018a.

Grosvenor, D. P., Sourdeval, O., Zuidema, P., Ackerman, A., Alexandrov, M. D., Bennartz, R., Boers, R., Cairns, B., Chiu, J. C., Christensen, M., Deneke, H. M., Diamond, M. S., Feingold, G., Fridlind, A., Hünerbein, A., Knist, C. L., Kollias, P., Marshak, A., McCoy, D., Merk, D., Painemal, D., Rausch, J., Rosenfeld, D., Russchenberg, H., Seifert, P., Sinclair, K., Stier, P., van Diedenhoven, B., Wendisch, M., Werner, F., Wood, R., Zhang, Z., and Quaas, J.: Remote sensing of droplet number concentration in warm clouds: A review of the current state of knowledge and perspectives, Rev. Geophys., doi:10.1029/2017RG000593, 2018b.

Gueymard, C. A.: The sun's total and spectral irradiance for solar energy applications and solar radiation models, Sol. Energy, 76, 423–453, 2004.

Hansen, J. and Travis, L.: Light scattering in planetary atmospheres, Space Sci. Rev., 16, 527–610, 1974.

Jacob, M., Ament, F., Gutleben, M., Konow, H., Mech, M., Wirth, M., and Crewell, S.: Investigating the liquid water path over the tropical Atlantic with synergistic airborne measurements, Atmos. Meas. Tech. Discus., 2019, 1–27, doi:10.5194/amt-2019-18, 2019.

Khain, A., Pinsky, M., Magaritz, L., Krasnov, O., and Russchenberg, H. W. J.: Combined observational and model investigations of the Z-LWC relationship in stratocumulus clouds, J. Appl. Meteorol. Clim., 47, 591–606, doi:10.1175/2007JAMC1701.1, 2008.

Kollias, P. and Albrecht, B.: Vertical velocity statistics in fair-weather cumuli at the ARM TWP Nauru climate research facility, J. Climate, 23, 6590–6604, doi:10.1175/2010JCLI3449.1, 2010.

Konow, H., Jacob, M., Ament, F., Crewell, S., Ewald, F., Hagen, M., Hirsch, L., Jansen, F., Mech, M., and Stevens, B.: A unified data set of airborne cloud remote sensing using the HALO Microwave Package (HAMP), Earth Syst. Sci. Data, 2018, 1–21, doi:10.5194/essd-2018-116, 2018.

Lamer, K., Kollias, P., and Nuijens, L.: Observations of the variability of shallow trade wind cumulus cloudiness and mass flux, J. Geophys. Res. Atmos., 120, 6161–6178, doi:10.1002/2014JD022950, 2014JD022950, 2015.

Lee, S.-S. and Feingold, G.: Aerosol effects on the cloud-field properties of tropical convective clouds, Atmos. Chem. Phys., 13, 6713–6726, doi:10.5194/acp-13-6713-2013, 2013.

Mace, G. G., Avey, S., Cooper, S., Lebsock, M., Tanelli, S., and Dobrowalski, G.: Retrieving co-occurring cloud and precipitation properties of warm marine boundary layer clouds with A-Train data, J. Geophys. Res. Atmos., 121, 4008–4033, doi:10.1002/2015JD023681, 2015JD023681, 2016.

Martin, G. M., Johnson, D. W., and Spice, A.: The measurement and parameterization of effective radius of droplets in warm stratocumulus clouds, J. Atmos. Sci., 51, 1823–1842, doi:10.1175/1520-0469(1994)051<1823:TMAPOE>2.0.CO;2, 1994.

McComiskey, A. and Feingold, G.: Quantifying error in the radiative forcing of the first aerosol indirect effect, Geophys. Res.Lett., 35, L02 810, doi:10.1029/2007GL032667, 2008.

5   Mech, M., Crewell, S., Meirold-Mautner, I., Prigent, C., and Chaboureau, J. P.: Information content of millimeter-wave observations for hydrometeor properties in mid-latitudes, IEEE T. Geosci. Remote, 45, 2287–2299, doi:10.1109/TGRS.2007.898261, 2007.

Mech, M., Orlandi, E., Crewell, S., Ament, F., Hirsch, L., Hagen, M., Peters, G., and Stevens, B.: HAMP - the microwave package on the High Altitude and LOng range research aircraft (HALO), Atmos. Meas. Tech., 7, 4539–4553, doi:10.5194/amt-7-4539-2014, 2014.

Merk, D., Deneke, H., Pospichal, B., and Seifert, P.: Investigation of the adiabatic assumption for estimating cloud micro- and macrophysical
10   properties from satellite and ground observations, Atmos. Chem. Phys., 16, 933–952, doi:10.5194/acp-16-933-2016, 2016.

Min, Q., Joseph, E., Lin, Y., Min, L., Yin, B., Daum, P. H., Kleinman, L. I., Wang, J., and Lee, Y.-N.: Comparison of MODIS cloud microphysical properties with in-situ measurements over the Southeast Pacific, Atmos. Chem. Phys., 12, 11 261–11 273, doi:10.5194/acp-12-11261-2012, 2012.

Minnis, P., Sun-Mack, S., Young, D. F., Heck, P. W., Garber, D. P., Chen, Y., Spangenberg, D. A., Arduini, R. F., Trepte, Q. Z., Smith, W. L.,
15   Ayers, J. K., Gibson, S. C., Miller, W. F., Hong, G., Chakrapani, V., Takano, Y., Liou, K. N., Xie, Y., and Yang, P.: CERES Edition-2 Cloud Property Retrievals Using TRMM VIRS and Terra and Aqua MODIS Data. Part I: Algorithms, IEEE Trans. Geosci. Remote Sens., 49, 4374–4400, doi:10.1109/TGRS.2011.2144601, 2011.

Nakajima, T. and King, M.: Determination of the optical thickness and effective particle radius of clouds from reflected solar radiation measurements. Part I: Theory, J. Atmos. Sci., 47, 1878–1893, 1990.

20   Oreopoulos, L. and Davies, R.: Plane parallel albedo biases from satellite observations. Part I: Dependence on resolution and other factors, J. Climate, 11, 919–932, 1998a.

Oreopoulos, L. and Davies, R.: Plane parallel albedo biases from satellite observations. Part II: Parameterization for bias removal, J. Climate, 11, 933–944, 1998b.

Painemal, D. and Zuidema, P.: Assessment of MODIS cloud effective radius and optical thickness retrievals over the Southeast Pacific with
25   VOCALS-REx in situ measurements, J. Geophys. Res. Atmos., 116, doi:10.1029/2011JD016155, d24206, 2011.

Pawlowska, H. and Brenguier, J.-L.: An observational study of drizzle formation in stratocumulus clouds for general circulation model (GCM) parameterizations, J. Geophys. Res. Atmos., 108, doi:10.1029/2002JD002679, 2003.

Platnick, S.: Vertical photon transport in cloud remote sensing problems, J. Geophys. Res., 105, 22 919–22 935, 2000.

Platnick, S. and Twomey, S.: Determining the susceptibility of cloud albedo to changes in droplet concentration with the Advanced Very
30   High Resolution Radiometer, J. Appl. Meteorol., 33, 334–347, 1994.

Platnick, S., Ackerman, S. A., Baum, B. A., Heidinger, A. K., Holz, R. E., King, M. D., Menzel, W. P., Nasiri, S., Weisz, E., and Yang, P.: Assessment of IDPS VIIRS cloud products and recommendations for EOS-era cloud climate data record continuity, Tech. Rep. , p. 57, NASA Goddard Space Flight Center, Greenbelt, MD, USA, https://jointmission.gsfc.nasa.gov/DEW_NPP_reports/VIIRS/Cloud/Products/Report/(Mar-19-2013).pdf, 2013.

35   Pontikis, C. and Hicks, E.: Contribution to the cloud droplet effective radius parameterization, Geophys. Res. Lett., 19, 2227–2230, doi:10.1029/92GL02283, 1992.

Pontikis, C. A.: Parameterization of the droplet effective radius of warm layer clouds, Geophys. Res. Lett., 23, 2629–2632, doi:10.1029/96GL02452, 1996.

Quaas, J., Boucher, O., and Lohmann, U.: Constraining the total aerosol indirect effect in the LMDZ and ECHAM4 GCMs using MODIS satellite data, Atmos. Chem. Phys., 6, 947–955, doi:10.5194/acp-6-947-2006, 2006.

Quaas, J., Ming, Y., Menon, S., Takemura, T., Wang, M., Penner, J. E., Gettelman, A., Lohmann, U., Bellouin, N., Boucher, O., Sayer, A. M., Thomas, G. E., McComiskey, A., Feingold, G., Hoose, C., Kristjansson, J. E., Liu, X., Balkanski, Y., Donner, L. J., Ginoux, P. A., Stier, P., Grandey, B., Feichter, J., Sednev, I., Bauer, S. E., Koch, D., Grainger, R. G., Kirkevag, A., Iversen, T., Seland, O., Easter, R., Ghan, S. J., Rasch, P. J., Morrison, H., Lamarque, J. F., Iacono, M. J., Kinne, S., and Schulz, M.: Aerosol indirect effects - general circulation model intercomparison and evaluation with satellite data, Atmos. Chem. Phys., 9, 8697–8717, doi:10.5194/acp-9-8697-2009, 2009.

Reid, J. S., Hobbs, P. V., Rangno, A. L., and Hegg, D. A.: Relationships between cloud droplet effective radius, liquid water content, and droplet concentration for warm clouds in Brazil embedded in biomass smoke, J. Geophys. Res. Atmos., 104, 6145–6153, doi:10.1029/1998JD200119, 1999.

Romps, D. M.: Exact Expression for the Lifting Condensation Level, J. Atmos. Sci., 74, 3891–3900, doi:10.1175/JAS-D-17-0102.1, 2017.

Rosenfeld, D.: Aerosol-cloud interactions control of Earth radiation and latent heat release budgets, Space Science Reviews, 125, 149–157, doi:10.1007/s11214-006-9053-6, 2006.

Schnitt, S., Orlandi, E., Mech, M., Ehrlich, A., and Crewell, S.: Characterization of Water Vapor and Clouds During the Next-Generation Aircraft Remote Sensing for Validation (NARVAL) South Studies, IEEE J. Sel. Top. Appl., 10, 3114–3124, doi:10.1109/JSTARS.2017.2687943, 2017.

Shettle, E.: Comments on the use of LOWTRAN in transmission calculations for sites with the ground elevated relative to sea level, Appl. Opt., 28, 1451–1452, 1989.

Siebert, H., Bethke, J., Bierwirth, E., Conrath, T., Dieckmann, K., Ditas, F., Ehrlich, A., Farrell, D., Hartmann, S., Izaguirre, M. A., Katzwinkel, J., Nuijens, L., Roberts, G., Schäfer, M., Shaw, R. A., Schmeissner, T., Serikov, I., Stevens, B., Stratmann, F., Wehner, B., Wendisch, M., Werner, F., and Wex, H.: The fine–scale structure of the trade wind cumuli over Barbados – an introduction to the CARRIBA project, Atmos. Chem. Phys., 13, 10061–10077, doi:10.5194/acp-13-10061-2013, 2013.

Stamnes, K., Tsay, S.-C., Wiscombe, W., and Laszlo, I.: DISORT, A General-Purpose Fortran Program for Discrete-Ordinate-Method Radiative Transfer in Scattering and Emitting Layered Media: Documentation of Methodology, Tech. rep., Dept. of Physics and Engineering Physics, Stevens Institute of Technology, Hoboken, NJ 07030, 2000.

Stephens, G.: Radiation profiles in extended water clouds. II: Parameterization schemes, J. Atmos. Sci., 35, 2123–2132, 1978.

Stevens, B., Ament, F., Bony, S., Crewell, S., Ewald, F., Groß, S., Hansen, A., Hirsch, L., Jacob, M., Kölling, T., Konow, H., Mayer, B., Wendisch, M., Wirth, M., Wolf, K., Bakan, S., Bauer-Pfundstein, M., Brück, M., Delanoë, J., Ehrlich, A., Farrell, D., Forde, M., Gödde, F., Grob, H., Hagen, M., Jäkel, E., Jansen, F., Klepp, C., Klingebiel, M., Mech, M., Peters, G., Rapp, M., Wing, E. A., and Zinner, T.: A high-altitude long-range aircraft configured as a cloud observatory - the NARVAL expeditions, B Am. Meterorol. Soc., to be submitted, 2018.

Twomey, S.: The influence of pollution on the shortwave albedo of clouds, J. Atmos. Sci., 34, 1149–1152, 1977.

vanZanten, M. C., Stevens, B., Vali, G., and Lenschow, D. H.: Observations of Drizzle in Nocturnal Marine Stratocumulus, J. Atmos. Sci., 62, 88–106, doi:10.1175/JAS-3355.1, 2005.

Warren, S., Hahn, C., London, J., Chervin, R., and Jenne, R.: Global distribution of total cloud cover and cloud type amounts over the ocean, Tech. rep., Boulder, CO, 1988.

Wendisch, M. and Brenguier, J.-L.: Airborne Measurements for Environmental Research – Methods and Instruments, Wiley–VCH Verlag GmbH & Co. KGaA, Weinheim, Germany, Weinheim, Germany, iSBN: 978-3-527-40996-9, 2013.

Wendisch, M. and Keil, A.: Discrepancies between measured and modeled solar and UV radiation within polluted boundary layer clouds, J. Geophys. Res., 104, 27 373–27 385, 1999.

Wendisch, M., Müller, D., Schell, D., and Heintzenberg, J.: An airborne spectral albedometer with active horizontal stabilization, J. Atmos. Oceanic Technol., 18, 1856–1866, 2001.

5 Wendisch, M., Yang, P., and Pilewskie, P.: Effects of ice crystal habit on thermal infrared radiative properties and forcing of cirrus, J. Geophys. Res., 112, D03 202, doi:10.1029/2006JD007899, 2007.

Wendisch, M., Pöschl, U., Andreae, M. O., Machado, L. A. T., Albrecht, R., Schlager, H., Rosenfeld, D., Martin, S. T., Abdelmonem, A., Afchine, A., Araujo, A., Artaxo, R., Aufmhoff, H., Barbosa, H. M. J., Borrmann, S., Braga, R., Buchholz, B., Cecchini, M. A., Costa, A., Curtius, J., Dollner, M., Dorf, M., Dreiling, V., Ebert, V., Ehrlich, A., Ewald, F., Fisch, G., Fix, A., Frank, F., Fütterer, D., Heckl, 10 C., Heidelberg, F., Hüneke, T., Jäkel, E., Järvinen, E., Jurkat, T., Kanter, S., Kästner, U., Kenntner, M., Kesselmeier, J., Klimach, T., Knecht, M., Kohl, R., Kölling, T., Krämer, M., Krüger, M., Krisna, T. C., Lavric, J. V., Longo, K., Mahnke, C., Manzi, A. O., Mayer, B., Mertes, S., Minikin, A., Molleker, S., Münch, S., Nillius, B., Pfeilsticker, K., Pöhlker, C., Roiger, A. E., Rose, D., Rosenow, D., Sauer, D., Schnaiter, M., Schneider, J., Schulz, C., de Souza, R. A. F., Spanu, A., Stock, P., Vila, D., Voigt, C., Walser, A., Walter, D., Weigel, R., Weinzierl, B., Werner, R., Yamasoe, M. A., Ziereis, H., Zinner, T., and Zöger, M.: The ACRIDICON-CHUVA campaign: Studying 15 tropical deep convective clouds and precipitation over Amazonia using the new German research aircraft HALO, Bull. Am. Meteorol. Soc., 97, 1885–1908, doi:10.1175/BAMS-D-14-00255.1, 2016.

Werner, F., Siebert, H., Pilewskie, P., Schmeissner, T., Shaw, R. A., and Wendisch, M.: New airborne retrieval approach for trade wind cumulus properties under overlying cirrus, J. Geophys. Res. Atmos., 118, 3634–3649, doi:10.1002/jgrd.50334, 2013.

Werner, F., Ditas, F., Siebert, H., Simmel, M., Wehner, B., Pilewskie, P., Schmeissner, T., Shaw, R. A., Hartmann, S., Wex, H., Roberts, G. C., 20 and Wendisch, M.: Twomey effect observed from collocated microphysical and remote sensing measurements over shallow cumulus, J. Geophys. Res., 119, 1534–1545, doi:10.1002/2013JD020131, 2014.

Wirth, M., Fix, A., Mahnke, P., Schwarzer, H., Schrandt, F., and Ehret, G.: The airborne multi-wavelength water vapor differential absorption lidar WALES: System design and performance, Appl. Phys. B.-Lasers O., 96, 201–213, 2009.

Wood, R.: Relationships between optical depth, liquid water path, droplet concentration and effective radius in an adiabatic layer cloud, 25 personal note, 2006.

Zeng, S., Riedi, J., Trepte, C. R., Winker, D. M., and Hu, Y.-X.: Study of global cloud droplet number concentration with A-Train satellites, Atmos. Chem. Phys., 14, 7125–7134, doi:10.5194/acp-14-7125-2014, 2014.